The spatial localisation of storm-time ULF waves due to plasmaspheric plumes and implications for calculating radial diffusion

Jasmine Kaur Sandhu[1], Kyle Robert Murphy[2], I. Jonathan Rae[3], Alexander William Degeling[4], Adnane Osmane[5], David Paul Hartley[6], and Leonid Olifer[7]

[1]University of Leicester
[2]Self
[3]Northumbria University
[4]Shandong University
[5]University of Helsinki
[6]University of Iowa
[7]University of Alberta

March 05, 2024

Abstract

The generation and propagation of Ultra Low Frequency (ULF) waves are intrinsically coupled to the cold plasma population in the terrestrial magnetosphere. During geomagnetic storms, extreme reconfigurations of the cold plasma creates a complex and dynamic system that drastically modifies this coupling. The extent and manner in which this coupling is affected remains an open question. In this report, we assess the coupling between ULF waves and cold plasmaspheric plumes during geomagnetic storms, and investigate the implications for ULF wave-driven radial transport of the outer radiation belt population. We present a series of event studies of Van Allen Probes observations. For each event, we use inferred measurements of the cold plasma density during plume crossings, in combination with magnetic and electric field observations of ULF waves. The event studies show very different, and at times contrasting, wave behaviour. This includes events where ULF waves appear to be spatially confined within plume structures. Initial estimates show that the localised patches of ULF wave power have significant implications for radial diffusion processes, and highlights the need for caution in estimating radial diffusion coefficients. We suggest that the cold plasma dynamics is an important source of uncertainty in radial diffusion models, and understanding cold plasma-ULF wave coupling is a critical area of future investigations.

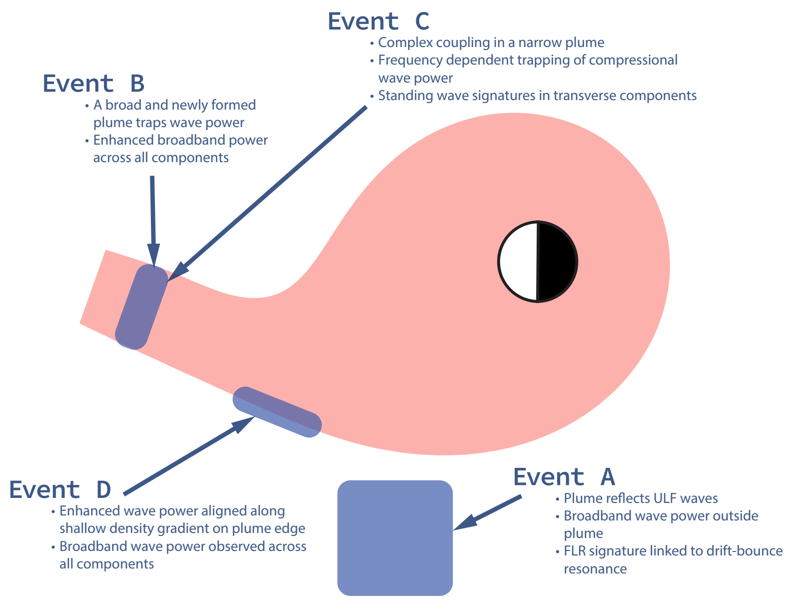
Event C
• Complex coupling in a narrow plume
• Frequency dependent trapping of compressional wave power
• Standing wave signatures in transverse components
Event B
• A broad and newly formed plume traps wave power
• Enhanced broadband power across all components
Event D
• Enhanced wave power aligned along shallow density gradient on plume edge
• Broadband wave power observed across all components
Event A
• Plume reflects ULF waves
• Broadband wave power outside plume
• FLR signature linked to drift-bounce resonance

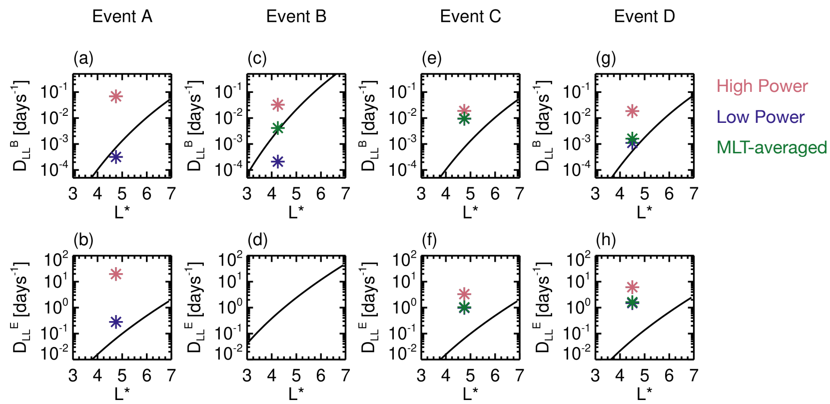
Event A
Event B
Event C
Event D
(a)
(b)
(c)
(d)
(e)
(f)
(g)
(h)
High Power
Low Power
MLT-averaged
L*
days⁻¹

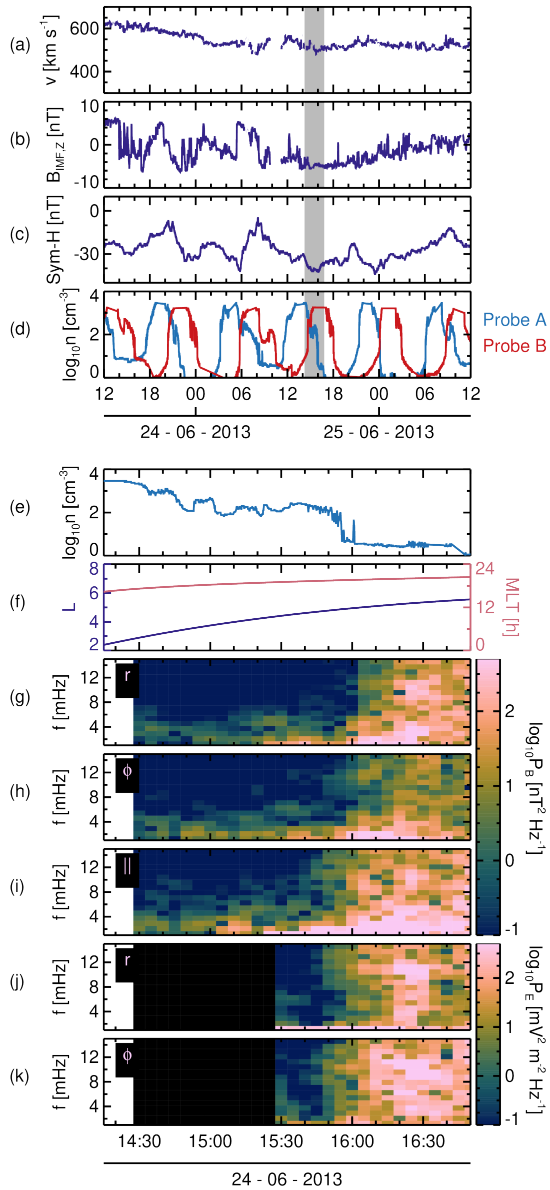

(a)
v [km s-1]
600
400
(b)
BIMF,Z [nT]
10
0
-10
(c)
Sym-H [nT]
0
-30
(d)
log10n [cm-3]
Probe A
Probe B
12 18 00 06 12 18 00 06 12
24 - 06 - 2013
25 - 06 - 2013
(e)
(f)
L
MLT [h]
(g)
(h)
(i)
(j)
(k)
f [mHz]
r
ϕ
||
log10PB [nT2 Hz-1]
log10PE [mV2 m-2 Hz-1]
14:30 15:00 15:30 16:00 16:30
24 - 06 - 2013

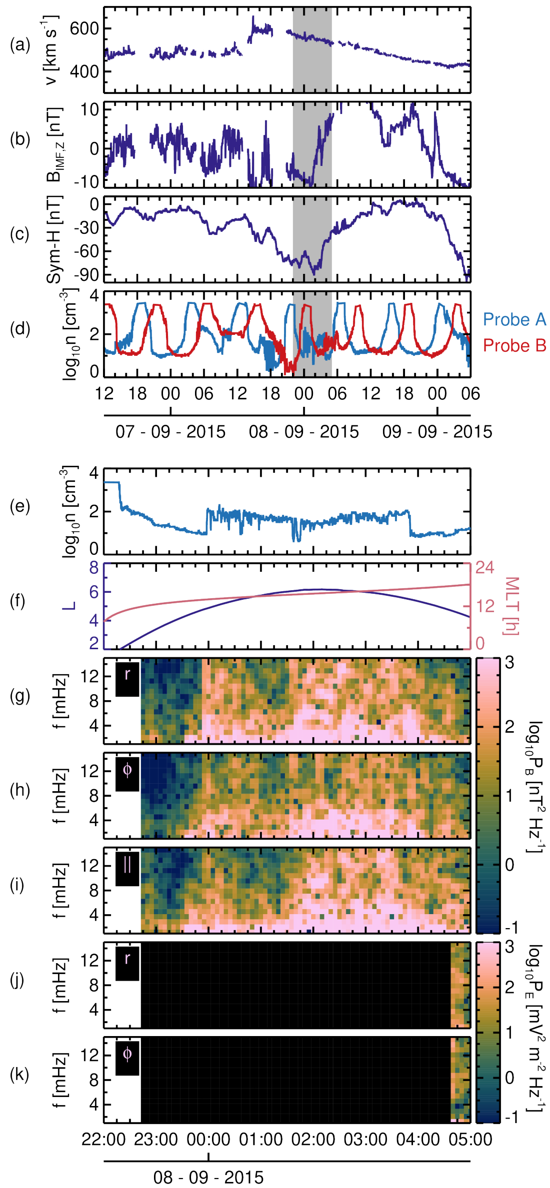

(a)
v [km s⁻¹]
600
400
(b)
B_IMF,Z [nT]
10
0
-10
(c)
Sym-H [nT]
0
-30
-60
-90
(d)
log10n [cm⁻³]
Probe A
Probe B
12 18 00 06 12 18 00 06 12 18 00 06
07 - 09 - 2015
08 - 09 - 2015
09 - 09 - 2015
(e)
log10n [cm⁻³]
(f)
L
MLT [h]
24
12
0
(g)
(h)
(i)
(j)
(k)
f [mHz]
r
ϕ
||
log10PB [nT² Hz⁻¹]
log10PE [mV² m⁻² Hz⁻¹]
22:00 23:00 00:00 01:00 02:00 03:00 04:00 05:00
08 - 09 - 2015

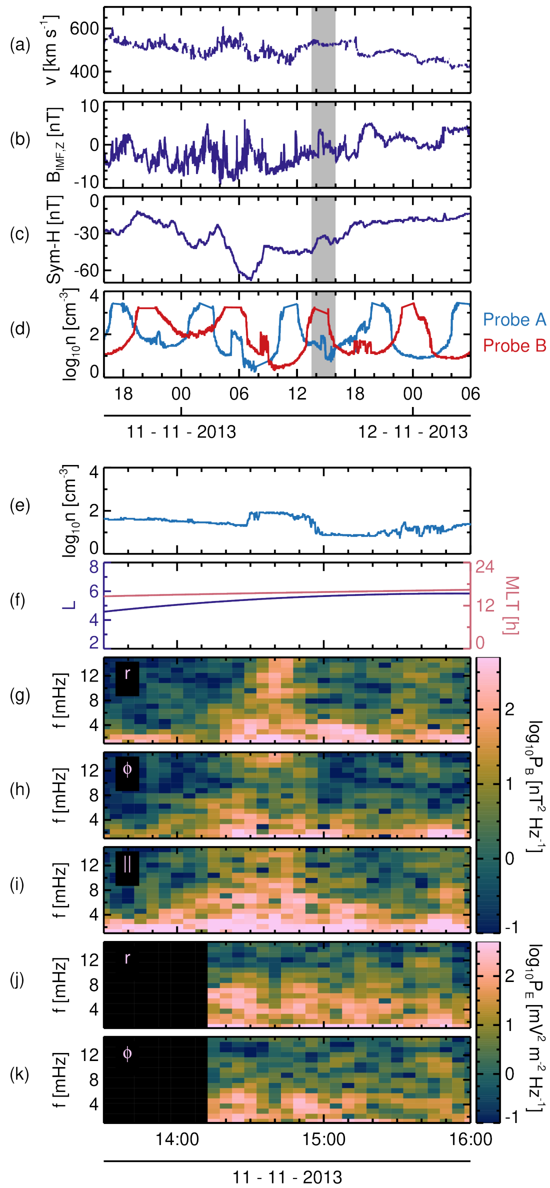
(a)
v [km s-1]
600
400
(b)
B IMF,Z [nT]
10
0
-10
(c)
Sym-H [nT]
0
-30
-60
(d)
log10n [cm-3]
4
2
0
Probe A
Probe B
18
00
06
12
18
00
06
11 - 11 - 2013
12 - 11 - 2013
(e)
log10n [cm-3]
(f)
L
MLT [h]
24
12
0
(g)
r
(h)
ϕ
(i)
||
(j)
r
(k)
ϕ
f [mHz]
12
8
4
log10PB [nT2 Hz-1]
log10PE [mV2 m-2 Hz-1]
14:00
15:00
16:00
11 - 11 - 2013

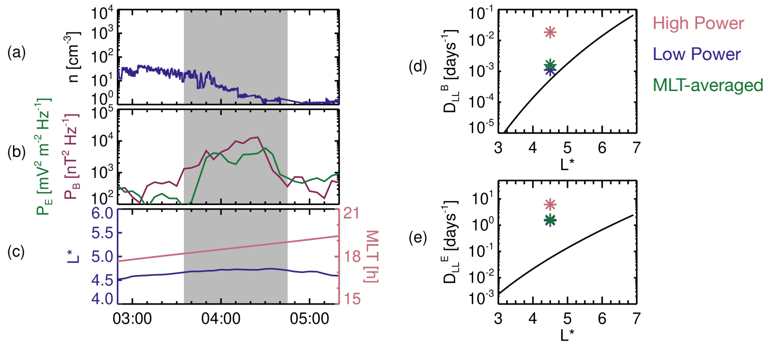
(a)
n [cm-3]
(b)
PE [mV2 m-2 Hz-1]
PB [nT2 Hz-1]
(c)
L*
MLT [h]
03:00
04:00
05:00
(d)
DLL B [days-1]
L*
High Power
Low Power
MLT-averaged
(e)
DLL E [days-1]
L*

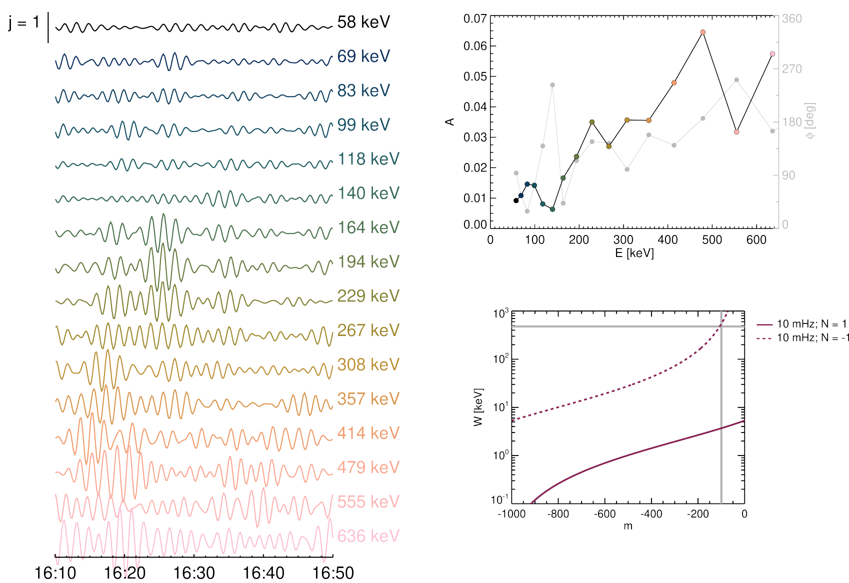
j = 1
58 keV
69 keV
83 keV
99 keV
118 keV
140 keV
164 keV
194 keV
229 keV
267 keV
308 keV
357 keV
414 keV
479 keV
555 keV
636 keV
16:10
16:20
16:30
16:40
16:50
A
E [keV]
ϕ [deg]
W [keV]
m
10 mHz; N = 1
10 mHz; N = -1

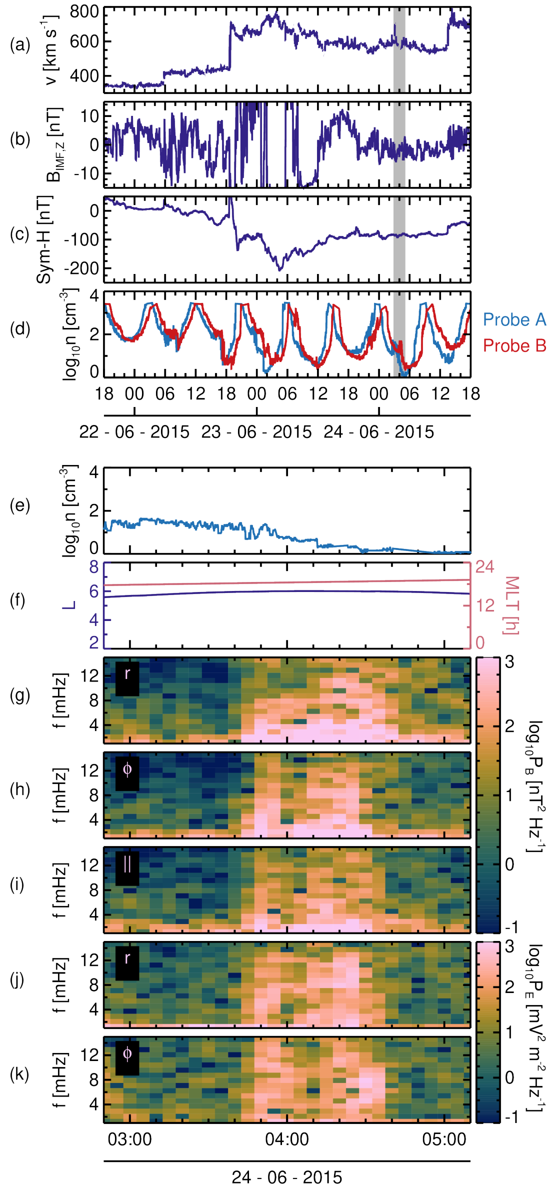

(a)
v [km s-1]
(b)
B_IMF,Z [nT]
(c)
Sym-H [nT]
(d)
log10n [cm-3]
Probe A
Probe B
22 - 06 - 2015
23 - 06 - 2015
24 - 06 - 2015
(e)
log10n [cm-3]
(f)
L
MLT [h]
(g)
(h)
(i)
(j)
(k)
f [mHz]
log10PB [nT2 Hz-1]
log10PE [mV2 m-2 Hz-1]
03:00
04:00
05:00
24 - 06 - 2015

The spatial localisation of storm-time ULF waves due to plasmaspheric plumes and implications for calculating radial diffusion

J. K. Sandhu[1,2], K. R. Murphy[2], I. J. Rae[2], A. W. Degeling[3], A. Osmane[4], D. P. Hartley[5], and L. Olifer[6]

[1]Department of Physics and Astronomy, University of Leicester, Leicester, UK
[2]Department of Maths, Physics and Electrical Engineering, Northumbria University, Newcastle Upon Tyne, UK
[3]Institute of Space Science, Shandong University, Weihai, China
[4]Department of Physics, University of Helsinki, Helsinki, Finland
[5]Department of Physics and Astronomy, University of Iowa, Iowa City, IA, USA
[6]Department of Physics, University of Alberta, Edmonton, AB, Canada

Key Points:

- Plasmaspheric plumes can spatially localise ULF wave power in the inner magnetosphere during geomagnetic storms.
- The coupling between the plumes and ULF waves is highly variable between events indicating a complex relationship.
- Cold plasma coupling is a crucial consideration in radial diffusion calculations and a source of uncertainty in current models

Corresponding author: J. K. Sandhu, jasmine.sandhu@leicester.ac.uk

Abstract

The generation and propagation of Ultra Low Frequency (ULF) waves are intrinsically coupled to the cold plasma population in the terrestrial magnetosphere. During geomagnetic storms, extreme reconfigurations of the cold plasma creates a complex and dynamic system that drastically modifies this coupling. The extent and manner in which this coupling is affected remains an open question. In this report, we assess the coupling between ULF waves and cold plasmaspheric plumes during geomagnetic storms, and investigate the implications for ULF wave-driven radial transport of the outer radiation belt population. We present a series of event studies of Van Allen Probes observations. For each event, we use inferred measurements of the cold plasma density during plume crossings, in combination with magnetic and electric field observations of ULF waves. The event studies show very different, and at times contrasting, wave behaviour. This includes events where ULF waves appear to be spatially confined within plume structures. Initial estimates show that the localised patches of ULF wave power have significant implications for radial diffusion processes, and highlights the need for caution in estimating radial diffusion coefficients. We suggest that the cold plasma dynamics is an important source of uncertainty in radial diffusion models, and understanding cold plasma-ULF wave coupling is a critical area of future investigations.

Plain Language Summary

The terrestrial magnetosphere is a highly dynamic environment around our Earth where populations of plasma are trapped within our global geomagnetic field. The plasma can interact with the magnetic field through a range of electromagnetic waves. In this study, we explore how the lowest energy plasma, termed the cold plasma population, can control how electromagnetic waves propagate through the system and dictate where their intensity is high. We focus on Ultra Low Frequency (ULF) waves that play a key role in transport of high energy electrons. Using spacecraft observations to observe both the waves and the cold plasma density, we present analysis of four events where cold plasma density structures resulted in the spatial localisation of the ULF waves. The four events showed very different, and at times contrasting, dependences that highlight the relationship between the cold plasma and ULF waves is variable and complex. Finally, we discuss implications for how ULF waves interact with the high energy plasma, and show that the presence of the cold plasma structures are a critical factor that should be accounted for when estimating the magnitude of ULF wave driven transport.

1 Introduction

Electromagnetic waves are the fundamental mode of energy propagation and transport across plasma in the terrestrial magnetosphere. These waves can be broadly categorised according to frequency (Jacobs et al., 1964), where perturbations with frequencies ranging between $\sim 1-10$ mHz are categorised as Ultra Low Frequency (ULF) waves. ULF waves are a vital component of magnetospheric dynamics, associated with auroral substorm processes (Smith et al., 2023), resonant acceleration of local plasma (A. W. Degeling et al., 2008; Hao et al., 2019; Ren et al., 2017), particle precipitation (Rae et al., 2018), and stochastic acceleration and transport driven by broadband ULF waves via radial diffusion (a critical element of radiation belt dynamics) (Turner et al., 2012; Elkington et al., 2003; Lejosne & Kollmann, 2020; Sandhu, Rae, Wygant, et al., 2021; Osmane et al., 2023).

Broadband ULF waves are primarily generated as external fast mode waves (e.g. magnetopause fluctuations driven by solar wind dynamic pressure, Kelvin-Helmholtz instabilities on the magnetopause flanks). The propagation of the fast mode waves in the inner magnetosphere is controlled by the global distribution of Alfvén speed, which is determined by both the background magnetic field and the plasma mass density. The

Alfvén speed distribution governs where fast mode waves can couple to shear Alfvén waves and drive Field Lines Resonances (FLRs), and sharp density gradients at the plasmapause can reflect/evanesce fast mode waves (Dungey, 1954; Southwood, 1974; Kivelson & Southwood, 1986). ULF waves can also be generated through internal sources, such as drift-bounce resonance with ring current ions driving FLRs, where the resonant frequency is again determined by the local Alfvén speed (Southwood, 1974). Both externally and internally driven ULF waves are intrinsically coupled to the Alfvén speed, and thus coupled directly to the cold plasma population. Therefore, changes in the cold plasma population can alter key characteristics and the propagation of ULF waves in the inner magnetosphere.

How does the coupling shape ULF wave phenomena during geomagnetic storms? It is well-established that elevated levels of convection during storms effectively erode cold plasma from the inner magnetosphere; the plasmasphere shrinks with a well-defined and sharp plasmapause, and a plasmaspheric plume can form in the afternoon sector (e.g., Chen & Wolf, 1972; Moldwin et al., 1994; Sandhu et al., 2017). The plume is high density plasma (~ 100 cm^{-3}) originating from the plasmasphere that, due to the increased convective electric field, is no longer within the Alfvén layer (or stagnation streamline between the corotating and convecting plasma flows). The plasma is convected towards the dayside and can simplistically be envisioned as a “strip” of high density plasma extending from the plasmasphere to the dayside magnetopause. During the lifetime of a plume, it progressively reduces in width and density (Goldstein et al., 2004; Darrouzet et al., 2009). Plumes introduce a localised region of high density plasma within a low density regime, as well as introducing azimuthal and radial density gradients that will be encountered along radiation belt electron drift orbits. Alongside these changes in the density of the plasma, the cold plasma population undergoes compositional variations with substantially increased concentrations of heavy ions that contribute significantly to the mass density and local Alfvén speed (e.g., Sandhu et al., 2017; James et al., 2021).

The drastic changes in the cold plasma mass density have serious implications for ULF wave phenomena and associated wave-particle interactions. For example, the global reduction in mass density and plasmapause erosion contributes to variations in FLR frequencies (Sandhu, Yeoman, & Rae, 2018; Wharton et al., 2020; Rae et al., 2019; Elsden, Yeoman, et al., 2022). Although these broad trends have been investigated, the specific physics and the role of plumes are comparatively under-explored. There are significant knowledge gaps in how ULF waves respond to plume structures, and whether the presence of plumes significantly alter storm-time ULF wave behaviour. Recent work has begun to unravel the problem as well as highlighting ULF wave - plume coupling as an emerging area of intriguing and unique physics. New results by Sandhu et al. (2023) show that plumes can significantly alter FLR polarisations, generating 3D FLRs (Elsden & Wright, 2022; Elsden, Wright, & Degeling, 2022). Event studies by Zhang et al. (2019) and Sandhu, Rae, Staples, et al. (2021), as well as modelling work by A. W. Degeling et al. (2018), have further demonstrated that plumes can be associated with localised enhancements in ULF wave power within the plume. Are these single event studies representative of ULF wave - plume coupling? And if so, what does a region of localised ULF wave power along an electron drift orbit mean for radiation belt dynamics? In this report, we present a selection of case studies to demonstrate that the ULF wave - plume coupling is complex and highly variable. We further explore consequences for ULF wave driven radial diffusion of radiation belt electrons.

2 Observations and Data Analysis

We present observations provided by the Van Allen Probes mission. The Van Allen Probes were two identically instrumented spacecraft (Probe A and Probe B) in a 9 hour period and 10 degree inclination orbit of the Earth, which operated between 2012 - 2019. Apogee and perigee was typically ~ 600 km and 5.8 R_E, respectively. The orbital apogee precessed through local time, spanning 24 hours of local time in less than 2 years. Due to the extensive 7 year data set covering a range of geomagnetic conditions and multiple geomagnetic storms, the data provided by the Van Allen Probes is a highly suitable choice for these investigations.

2.1 ULF Wave Observations

This study employs magnetic field observations from the Electric and Magnetic Field Instrument Suite and Integrated Science (EMFISIS) instrument (Kletzing et al., 2013, 2023) and electric field observations from the Electric Field and Waves (EFW) instrument (Wygant et al., 2013). It is noted that the EFW instrument is highly susceptible to data gaps due to contamination by spacecraft charging effects amongst other error sources (Breneman et al., 2022), and some events shown here include EFW data gaps as a result.

The magnetic and electric field measurements allow for ULF wave identification and characterisation using the method below, following the analysis of Sandhu, Rae, Wygant, et al. (2021) and Murphy et al. (2023).

1. The background field is estimated as the running average over a 20 minute sliding window that is incremented by 1 minute, and subtracted from the field measurements to obtain the residual field.
2. The residual field is transformed to a magnetic field-aligned coordinate system. The parallel component is aligned with the background field, the toroidal component is eastwards and perpendicular to the geocentric position vector, and the poloidal component completes the Cartesian system.
3. The power spectral density is computed using a Fourier Transform over a 20 minute sliding window that is incremented by 5 minutes. We employ power spectral densities calculated by Murphy et al. (2023), where magnetic field perturbations associated with the rapidly varying background field encountered by the spacecraft near perigee are removed.

The approach provides observations of power spectral density, and we focus on a ULF wave frequency range between $1 - 15$ mHz.

2.2 Plume Identifications

Measurements of the total electron density are inferred from identifications of the upper hybrid resonance frequency from EMFISIS electric field observations (Kurth et al., 2015). Timeseries of the electron density can be used to identify instances of plasmapause and plume boundary crossings, and we employed the Hartley (2022) database of Van Allen Probes plume crossings. A separate storm list (Walach, 2023) was consulted to focus exclusively on storm time plume crossings. Quiet times were omitted as the relative absence of ULF wave activity (compared to storm times (Sandhu, Rae, Wygant, et al., 2021; Murphy et al., 2023)) means it would be challenging to explore how the waves couple to plumes. From an analysis of the plume crossings, we observed a variety of forms of coupling and a selection of the events are presented here.

3 Results

Four events are presented here to demonstrate the widely variable nature of ULF wave and cold plasma coupling. In Figure 1 we provide a schematic illustration showing where enhanced and spatially localised enhanced ULF wave power is observed relative to the plume for each event. We note that all plume events are located in the afternoon or dusk MLT sector, in line with peak occurrence of plume observations (Darrouzet et al., 2008). We now review the ULF wave observations (magnetic and electric fields) for each event in detail, where the events taken together exemplify the variable nature of the ULF wave coupling to the cold plasma plumes.

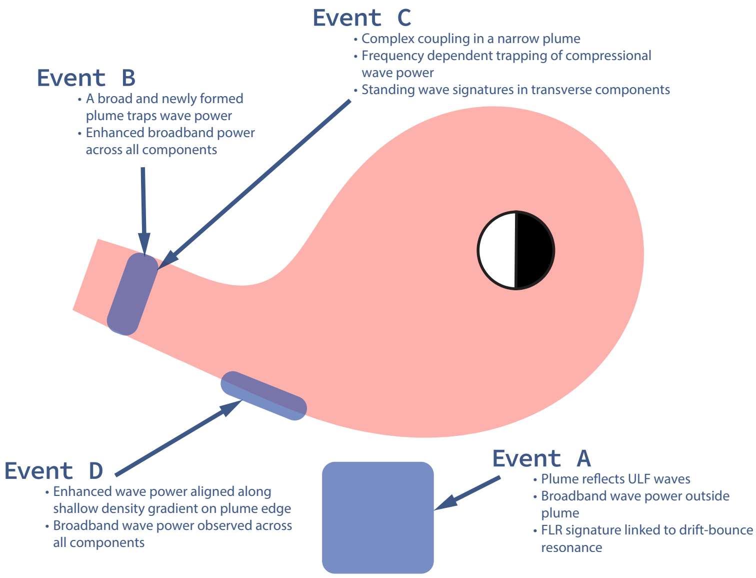

Figure 1. Schematic illustrating the spatial locations of enhanced ULF wave power for each event relative to the plume. The plasmasphere and plume is shown as the shaded coral region, and is intended only as a rough visual aid. Regions on enhanced wave power are depicted as shaded blue regions. The labels correspond to events described in the main text, and key points relating to each event are noted.

For each event we only show observations from Van Allen Probe A over a single plume crossing. Observations from Van Allen Probe B were analysed as part of the analysis to verify that key changes observed by Probe A were predominantly spatial dependences, but are now included here for brevity. For all events shown, the corresponding observations from Probe B that was located in a different region did not show ULF wave enhancements at the same time, and we confidently deduce that the enhancements discussed are not global temporal variations. We restricted analysis to a single pass, as it is outside of the scope here to examine the ULF waves alongside the temporal evolution of these plumes. We intend to present a separate and more detailed analysis of evolution, particle interactions, and reconstructions of the events in subsequent papers.

3.1 Event A: A Plume Blocks Wave Propagation

Figure 2 shows an overview of Event A on 24 June 2013. Panels (a-d) shows contextual solar wind, geomagnetic activity, and density observations over a 2 day interval, whereas panels (e-k) focus on the single plume crossing over a ~ 3 hour interval where detail on the ULF wave and density observations can be clearly observed.

Solar wind conditions are shown in panel (a) for the solar wind speed, v [km s^{-1}], and panel (b) for the southward component of the Interplanetary Magnetic Field (IMF), $B_{\mathrm{IMF,z}}$ [nT]. We observe a steady solar wind speed of 500 - 600 km s^{-1} throughout the interval. The southward IMF component is variable, switching from northward to southward, until remaining weakly southward from 08:00 24 June 2013. Panel (c) shows the Sym-H index [nT] to indicate the level of geomagnetic activity generally associated with the ring current population (Iyemori, 1990; Sandhu, Rae, & Walach, 2021). We observe a series of moderately negative Sym-H excursions reaching just below -40 nT. Panel (d) shows the total electron density for Probe A (blue) and Probe B (red), where the Probes had an orbital apogee in the dusk sector. The density time series exhibits significant variability, with the density profile changing notably from pass to pass. We see a clear bulge observed at approximately $06 - 08$ UT, which then detaches to form a distinct plume structure (see Probe B pass at ~ 10 UT). The plume and bulge are highly variable, with the observed size having reduced on each subsequent pass. A couple of hours after formation, the plume has subsided considerably (see Probe B pass at ~ 18 UT).

We now focus on the Probe A traversal of the plume between 14:15 to 16:45 UT 24 June 2013. For this interval, Probe A is approaching apogee and is located in the dusk sector (panel (f)). Panel (e) shows the density timeseries, where we observe initially high plasmaspheric densities (< 100 cm^{-3}) between $\sim 14:15-14:50$ UT. There is then a transition region where densities hover around 100 cm^{-3} ($\sim 14:15-16:00$ UT), followed by a sharp drop at $16:00$ UT to low plasmatrough-like densities of a few cm^{-3}. It is difficult to ascertain from the in situ measurements, but the density profiles (panels (d) and (e)) suggest the plume is in the process of detaching/merging with the plasmasphere. Plasmapause simulations by Goldstein et al. (2014) predict the presence of a plume that extends to the dayside magnetopause, and these simulations are highly valued at providing contextual information on the global structure of the cold plasma population.

Panels (g-k) show the observed ULF wave power across the plume structure. There is a sharp increase in broadband ULF wave power across the plume boundary at 16 UT in the low density region, which is observed for all components. Wave power is enhanced over multiple orders of magnitude, increasing from ~ 1 nT^2 Hz^{-1} (~ 1 mV^2 m^{-2} Hz^{-1}) up to more than ~ 100 nT^2 Hz^{-1} (~ 100 mV^2 m^{-2} Hz^{-1}) for the magnetic (electric) field ULF waves. The signature is particularly prominent in the electric field components (panels (j,k)). The magnetic field components at low frequencies ($\sim 1 - 2$ mHz) appear to be unconstrained by the plume edge, and instead indicate the presence of a potential narrow band structure. The azimuthal electric field component (panel (k)) exhibits a high power structure/band at approximately 10 mHz, reminiscent of an FLR signature.

The observations show clear and dramatic variations in ULF wave activity across the plume boundary, with the high density plume region devoid of both broadband and

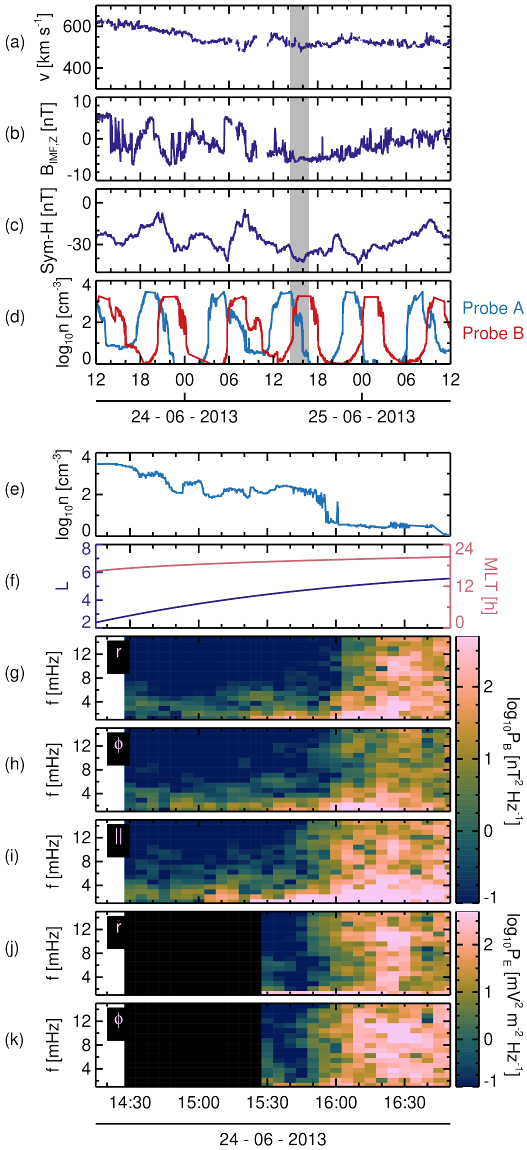

Figure 2. Time series from 12:00 23 June to 12:00 25 June 2013 of (a) solar wind speed, v [km s^{-1}], (b) north-south component of the Interplanetary Magnetic Field, $B_{\mathrm{IMF,Z}}$ [nT], (c) Sym-H index [nT], and (d) electron density, n [cm^{-3}] measured by Van Allen Probe A (blue) and Van Allen Probe B (red). Panels (e-k) show Van Allen Probes A observations for a shorter time interval from 14:15 to 16:45 24 June 2013 (as indicated by the grey shaded regions in panels (a-d)). The electron density, n [cm^{-3}], is shown in panel (e). The position of the spacecraft in L (indigo) and Magnetic Local Time (MLT, rose) is shown in panel (f). The magnetic field power, $P_{\mathbf{B}}$ [nT^2 Hz^{-1}], as a function of time and frequency, f [mHz], is shown for the (g) radial, (h) azimuthal, and (i) parallel field components. The electric field power, $P_{\mathbf{E}}$ [mV^2 m^{-2} Hz^{-1}], as a function of time and frequency, f [mHz], is shown for the (j) radial and (k) azimuthal field components.

FLR-like wave power enhancements. We suggest that the sharp density gradient at the plume edge is reflecting a large proportion of propagating compressional ULF waves, similarly to the reflective capability of a typical sharp plasmapause gradient (Abe et al., 2006). The result is that high ULF wave power in the low density plasmatrough region is excluded from accessing and propagating within the plume and lower radial distances. It is intriguing that the low frequency ULF waves do not appear to undergo significant reflection (panel (i)), contrasting results by e.g. Lee et al. (2002) that suggest lower frequency ULF waves have a higher probability of reflection. Instead the results agree with model outputs by A. W. Degeling et al. (2018) (see Figure 4), which shows high frequency exclusion and low frequency penetration of fast mode waves when a plasmaspheric plume is well-developed.

This event suggests that plumes are capable of inhibiting ULF wave propagation to low L values during geomagnetic storms. This contrasts to work showing how plasmapause erosion and ring current driven weakening of the magnetic field in the storm-time inner magnetosphere results in a large-scale depression of the Alfvén continuum (Sandhu, Yeoman, & Rae, 2018; Wharton et al., 2020), and consequently can allow ULF waves to penetrate to low L values during storm times (Rae et al., 2019). Instead, this event suggests that plumes can prohibit this increased ULF wave accessibility, at least across the MLT width that they exist.

The poloidal FLR signature observed at ~ 10 mHz in the azimuthal electric field (panel (k)) is in line with the peak occurrence of poloidal FLRs associated with drift-bounce resonance of ULF waves with substorm injected ions (James et al., 2013). Both prior to and during the event, ground magnetometer auroral indices exhibit substorm signatures (not shown), and substorm occurrences were also identified in both the Forsyth et al. (2015) and Newell and Gjerloev (2011) substorm lists. To investigate the 10 mHz feature more closely, we consult observations from the Magnetic Ion Electron Spectrometer (MagEIS) instrument (Blake et al., 2013) for this event. The analysis is detailed further in S1 of the Supporting Information. In brief, we observe characteristic features of drift resonance with ~ 500 keV protons, including high amplitude periodic oscillations and a 180 degree phase shift across the resonant energy. We suggest that the low density environment allows a spatial localisation of the resonant interaction by providing local field lines with eigenfrequencies capable of meeting the resonance condition (Zhang et al., 2019). The high mass densities in the plume region significantly alter the field line eigenfrequencies and prevent FLR driving. We also note that the plume density gradients can significantly distort the resonant zone, introducing a "kink" to lower L values at the dusk sector (e.g. see Figure 2 of A. W. Degeling et al. (2018)) and increasing the likelihood of poloidally polarised FLRs in this region. The analysis of MagEIS data for this event is highlighted here as brief example of how internally driven ULF waves can contribute to key storm time wave dynamics, as well as externally driven broadband perturbations. It also demonstrates how detailed event study analysis can be fruitful in exploring a range of ULF wave drivers that may be lost in a broad statistical analysis. There is a significant scope to conduct highly detailed multi-instrument analysis for each event, assessing particle dynamics over all observed energies, although due to space constraints we consider only MagEIS observations for this event.

3.2 Event B: A Broad Plume Traps ULF Waves

Timeseries for this event are shown in Figure 3, using the same format as Figure 2 where panels (a-d) show the longer period variations over a multi-day interval and panels (e-k) focus on one plume structure crossing. For this event, the solar wind speed varies between 500 to 600 km $^{-1}$ (panel (a)) with a variable southward IMF component (panel (b)). At approximately 02 UT 08 September, $B_{\mathrm{IMF,z}}$ rotates from strongly southward (~ -10 nT) to strongly northward (~ 10 nT). The period is associated with a strong geomagnetic disturbance, where panel (c) shows the Sym-H index decreases to nearly -90 nT within roughly a day followed by a rapid recovery in less than a day. This storm contrasts to the typical features of a classic geomagnetic storm (rapid main phase and prolonged multi-day recovery (Hutchinson et al., 2011)), where it appears the northward $B_{\mathrm{IMF,z}}$ rotation halts ring current energisation and allows decay processes to dominate. This event is a subset of a longer period series of geomagnetic disturbances driven by multiple CME interactions, resulting in complex radiation belt dynamics (Staples et al., 2022, and others).

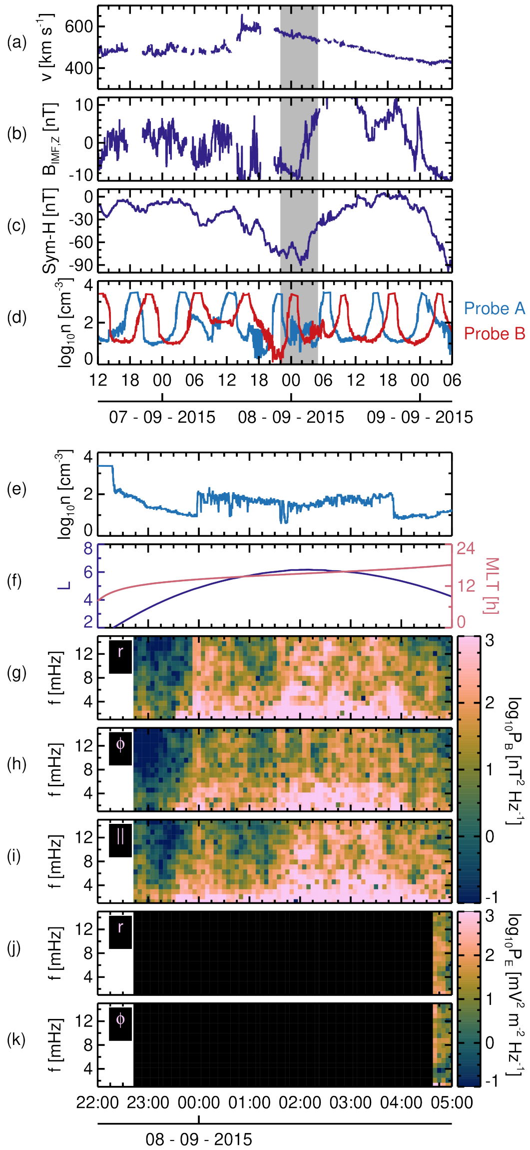

Figure 3. Time series in the same format as Figure 2, for (a-d) 12:00 06 September to 06:00 09 September 2015, and (e-k) 22:00 07 September to 05:00 08 September 2015.

For this event, the Probes had an apogee in the afternoon sector, and the in situ density measurements show high variability in the cold plasma population throughout the geomagnetic disturbance (panel (d)). At the beginning of the event, both Probes sample a typical plasmasphere and a relatively dense plasmatrough. Plasmatrough densities are ~ 10 cm^{-3}, and could potentially instead be a region of an extended and diffuse plasmasphere. At $\sim$ 04 UT 07 September, the Sym-H index has a small depression to ~ -50 nT and the density profile from Probe A indicates the presence of a plasmaspheric bulge. On the subsequent pass for Probe A, the bulge has departed from the plasmasphere and a clear plume structure is observed at approximately 16 UT. The plume structure is highly variable in thickness and density across each Probe traversal. The plume is observed until $\sim$ 06 UT 08 September, when Probe A observes only a high density plasmatrough in place of the plume with densities of $\sim$ 10 cm^{-3}, indicating that the inner magnetospheric density distribution has returned to its original state.

Panels (e-k) focus on the Probe A crossing of the plume between 22 UT 07 September to 05 UT 08 September 2015, where Probe A is sampling the broad and newly formed plume at the peak of the geomagnetic disturbance. For this interval, the probe is undergoing an apogee pass through the afternoon sector (panel (f)). The density profile shows the plume is spatially extensive, with Probe A sampling the plume over 4 hours and an estimated azimuthal width of 2.9 hours in MLT. The density within the plume is approximately 100 cm^{-3}, although there is significant substructure within the plume evidenced by a "jagged" timeseries. The density gradients on the plume edges are sharp, and the density reduces to less than 10 cm^{-3} in the plasmatrough.

Panels (g-k) show ULF wave power variations. We note that although there is a lack of electric field data for this event (panels (j,k)), the magnetic field data alone provides worthwhile discussion. All magnetic field components exhibit enhancements in the wave power within the plume region (panels (g-i), 00 - 04 UT). The enhancements are observed over a wide frequency range from 1 to 15 mHz, with wave power reaching values up to $\sim 10^3$ nT^2 Hz^{-1}. Furthermore, frequency profiles of the wave power (not shown) indicate a relatively stable peak in azimuthal component power at approximately 4 mHz, evidencing a potential standing wave structure. This feature is somewhat masked by the coincident broadband enhancements in panel (h).

Outside the plume, the power drops markedly by 2 - 3 order of magnitude ($\sim$ 1 nT^2 Hz^{-1}), most noticeable on the noonside of the crossing at 00 UT. At the dusk side crossing at 04 UT, although the transverse components exhibit a clear decrease in power, the compressional component displays similarly high wave power into the plasmatrough for the remainder of the interval shown (panel (i)). We have not extended the time range for panel (i) further than shown as the Probe is rapidly approaching perigee and moving into a low L region, such that it would be inappropriate to compare and attribute changes solely due to the plume boundary.

We interpret observations shown in Figure 3 as evidence of ULF wave power being trapped and confined within a plume, similar to the event shown by Sandhu, Rae, Staples, et al. (2021) (see Figure 5) and the simulation results by A. W. Degeling et al. (2018). We suggest that the sharp density gradients at the edges of the plume reflect ULF waves and confine them within the high density region, acting like a miniature wave cavity.

3.3 Event C: Complex Coupling in a Narrow Plume

Following the same format as Figure 2, Figure 4 shows observations of solar wind, geomagnetic activity and in situ density and ULF wave power. For this event, the solar wind speed is relatively steady (panel (a)) and $B_{\mathrm{IMF,z}}$ is generally southward but variable in magnitude (panel (b)). Panel (c) shows the occurrence of a moderate geomagnetic storm with Sym-H minimum of approximately -70 nT at 07 UT 11 November. Probe A and Probe B have apogees located in the dusk sector. Panel (d) shows initially high densities of $\sim$ 100 cm^{-3} and above, with an extended and diffuse plasmasphere. From $\sim$ 04 UT 11 November, there is a dramatic depletion of density, where a distinct plume has formed and the plasmasphere has been eroded to within the Probes orbital coverage, such that the probes now sample plasmatrough densities of a few cm^{-3}. The Probes encounter multiple passes of the plume over subsequent orbits, where we observe a thinning of the plume with time. From 21 UT 11 November, the plume has eroded and is no longer visible.

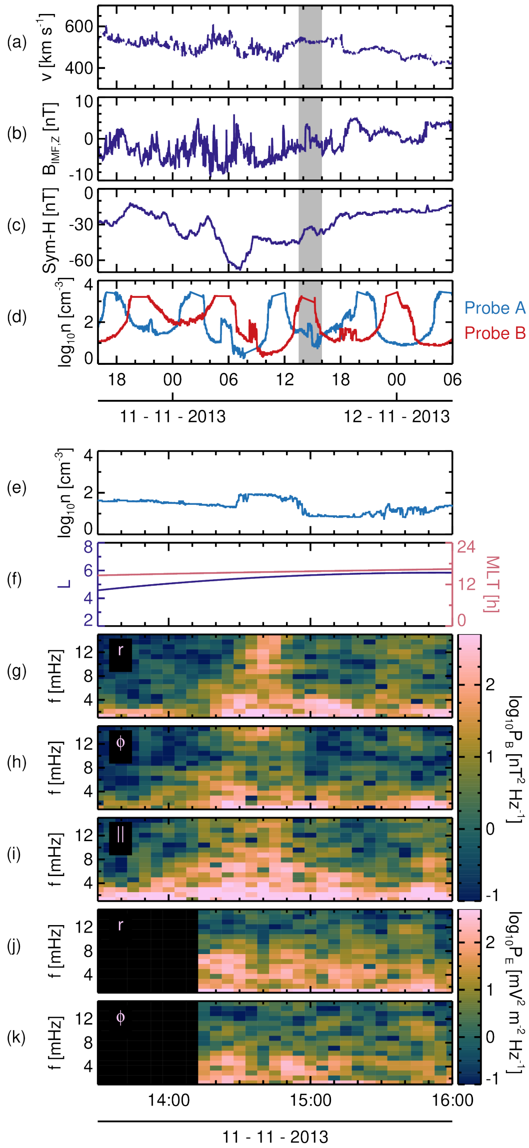

Figure 4. Time series in the same format as Figure 2, for (a-d) 16:00 10 November to 06:00 12 November 2013, and (e-k) 13:30 to 16:00 11 November 2013.

Panels (e-k) focus on a Probe A crossing of the eroding plume between 13:30 to 16:00 UT 11 November. Panel (e) shows the plume is thin (compare to Figure 3e), with density changes of less than one order of magnitude. The density inside the plume is $\sim$ 100 cm^{-3} and is located in the afternoon sector. The estimated azimuthal width in MLT is 0.6 hours. The plasmatrough densities outside the plume are $\sim$ 10 cm^{-3}.

The wave activity is complex and multi-faceted for this event. Panel (i) shows the compressional wave power at low frequencies ($<$ 4 mHz) is enhanced across the interval, and indicates limited dependences on being inside or outside of the plume structure. At higher frequencies (~ 8 mHz), there is a weak dependence for the compressional component, such that there is higher wave power (~ 100 nT^2 Hz^{-1}) inside the plume compared to outside the plume (~ 10 nT^2 Hz^{-1}). The higher frequency perturbations have comparatively shorter wavelengths than the low frequency ULF waves, and hence will be easier to confine within the small scale of the plume structure. The transverse components, particularly for the electric field component (panels (j,k)), indicate localised enhancements with high power located roughly at the plume boundaries at frequencies from approximately 1 to 8 mHz. This can be identified at ∼14:25 and ∼14:55 in Figure 4j,k.

The observations draw some similarities with magnetohydrodynamic (MHD) modelling results from A. W. Degeling et al. (2018), where constructive interference of compressional ULF waves within a plume generate a standing wave structure with the reflective plume boundaries forming nodes. Both these observations and the A. W. Degeling et al. (2018) model outputs note a resulting enhancement in radial electric field along the plume edge as a consequence of the eigenmode structure across the plume. However, the plume observed here exhibits relatively subdued density gradients at the edges (panel (e)) that would be relatively less effective at efficiently reflecting ULF waves. Furthermore, the spectrogram features in Figure 4 are broad in temporal space such that it is difficult to make certain conclusions form this event. Regardless, the complexity of the power spectra for even an "old" plume are certainly of interest. Furthermore, MagEIS particle observations for this event (not shown) indicate notable periodicity in field-aligned proton fluxes at 100 keV, suggesting potentially ULF wave modulated particle precipitation at the plume. The results highlight that plumes in later stages of evolution remain critical to shaping wave-particle interactions in the inner magnetosphere.

3.4 Event D: A Diffuse Edge Hosts Wave Power

Figure 5 shows observations for the final event, where an enhancement in wave power is observed along the plume boundary. Panels (a-d) show contextual information between 18 UT 21 June to 18 UT 24 June 2015. We observe the arrival of a solar wind structure at approximately 18 UT 22 June, evident from the rapid elevation of solar wind speed from ~ 400 to ~ 700 km s^{-1} (panel (a)). The IMF is variable with $B_{\mathrm{IMF,z}}$ magnitudes of around 10 nT and no consistent orientation (panel (b)). From approximately 18 UT 23 June, $B_{\mathrm{IMF,z}}$ stabilises around 0 nT and the solar wind speed is steady at approximately 600 km s^{-1}. The external solar wind driving generates a strong geomagnetic storm, with a Sym-H minimum of approximately -200 nT at 04 UT 23 June (panel (c)). Panel (d) shows density observations from the Probes, where apogee is in the dusk sector. The density in the inner magnetosphere is initially high ($\gtrsim 100$ cm^{-3}), with an extended plasmapause observed until 12 UT 22 June. On the following pass (~ 18 UT 22 June), the Sym-H index indicates the storm has entered the main phase (panel (c)), and both Probes now sample a low density plasmatrough with densities depleted to a few particles cm^{-3}. There are signatures of plume formation, although the plume is transient from pass to pass. At approximately 04 UT 24 June, during the late recovery phase, both Probes observe a plume feature. Due to the relatively stable solar wind conditions compared to the inital and main phase plumes, this crossing is ideal for in situ analysis.

Panels (e-k) focus on the plume crossing by Probe A between 02:50 to 05:10 24 June 2015. The probe samples the dusk-side edge of the plume, with densities of nearly 100 cm^{-3} inside the plume (3:10 UT) and reducing to nearly 0 cm^{-3} outside of the plume (05:00 UT), referring to panel (e). In contrast to the previous events (Figures 2, 3, and 4), the plume gradient is remarkably shallow and attributed to the old-age of the plume in the late recovery phase (Borovsky & Denton, 2008).

Panels (g-k) show the magnetic and electric field power spectra. We observe enhancements across all components and across a wide frequency range (1 to 12 mHz) lo-

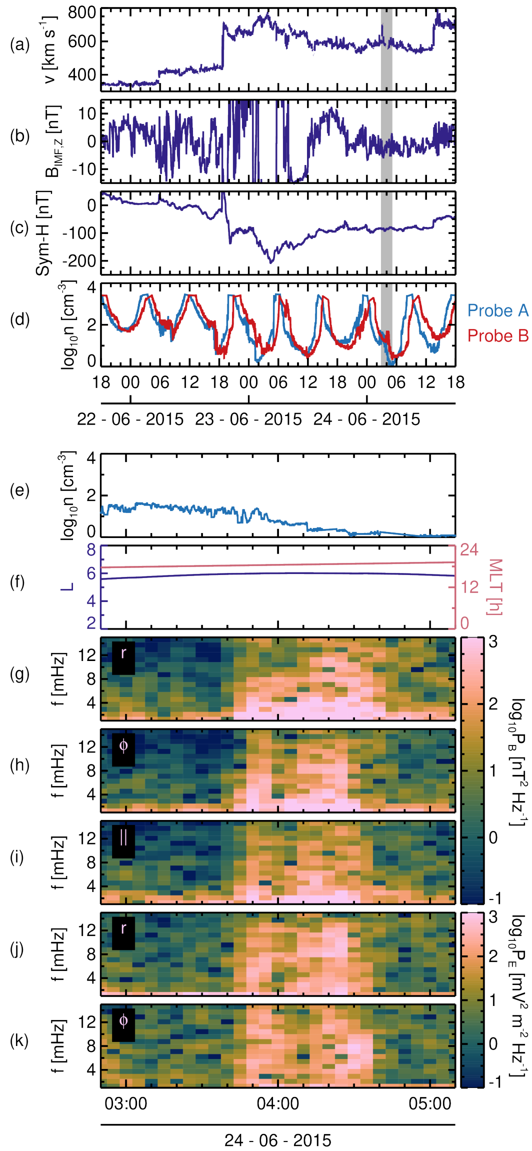

Figure 5. Time series in the same format as Figure 2, for (a-d) 18:00 21 June to 18:00 24 June 2015, and (e-k) 02:50 to 05:10 on 24 June 2015.

calised to the shallow gradient at the plume edge (between $\sim$ 3:45 to $\sim$ 4:40). Simultaneous observations of 470 keV electrons (not shown) are indicative of drift-bounce resonance, potentially driving ULF waves. As the local field line eigenfrequency is determined by the spatial distribution of electron density (Sandhu, Yeoman, James, et al., 2018), we suggest that only the region along the plume edge, where $n \sim 10$ cm^{-3} has field line eigenfrequencies that satisfy the resonance condition (Zhang et al., 2019). However, although this would generate localised enhancements in ULF wave power along the plume edge, the enhancement would be at a discrete poloidal frequency band. In contrast, panels (g-k) show broadband enhancements across all components. We do not fully understand the driver behind the spatial localisation observed here. We welcome community input, and simulation work will be conducted as part of future analysis to establish the physical processes at play.

4 Discussion

We have presented a selection of events, where each event shows distinct ULF wave coupling to the cold plasma population. The intention of this report is to highlight the range of variability across events - some plumes are capable of trapping high amplitude and broadband ULF waves (Events B, C, D), whereas other plumes have the opposite effect and are devoid of wave power (Event A). Although plumes are commonplace during storms (Darrouzet et al., 2009), it is now clearly a complex problem to predict the spatial distribution of the ULF wave power in the presence of these plumes. We hope to understand the sources and drivers of variability in future studies through detailed statistical investigation. We will focus on how plume properties (width, boundary gradients, magnitude of densities, and location) combine with ULF wave drivers (internal or external) combine to generate the observed variability exhibited here.

The results have confirmed that ULF wave propagation is highly coupled to the presence of plumes. But what are the implications for ULF wave impacts on inner magnetospheric dynamics? The regions of enhanced wave power can shape local processes, such as ULF wave induced precipitation (e.g., Event C), and are evidence of effective ring current decay through resonant interactions driving FLRs (e.g., Event A).

As well as local processes, ULF waves play a key role in the large-scale radial diffusion of energetic electrons in the outer radiation belt. In the next sub-section, we discuss how the ULF wave coupling to storm-time plumes can influence radial diffusion.

4.1 Implications for Estimating Radial Diffusion

In brief, ULF wave driven radial diffusion arises due to the electric and magnetic field wave periods being comparable to radiation belt electron drift periods. The (drift) resonant wave-particle interactions violate the third adiabatic invariant, and the fluctuations from broadband ULF wave activity “scatter” electrons radially inwards and outwards onto new drift paths (Fälthammar, 1965; Kellogg, 1959; Parker, 1960). The process is particularly efficient at reducing/smoothing radial phase space density gradients that can arise due to local wave-particle interactions or flux dropouts at the outer boundary. The acceleration by radial diffusion has been suggested to be dominant in the recovery phase of geomagnetic storms (Katsavrias et al., 2019; Jaynes et al., 2018), and the outward transport can contribute significantly to magnetopause shadowing (Turner et al., 2012; George et al., 2022). In brief, radial diffusion by ULF waves significantly contributes to the radial redistribution, energisation, and loss of radiation belt electrons.

The magnitude of ULF driven radial diffusion can be represented through a radial diffusion coefficient, D_{LL}, and models of D_{LL} are included in radiation belt modelling and forecasting tools in an attempt to capture the ULF wave contributions to radial transport. Commonly used empirical models of D_{LL} are based on statistical databases of ULF wave power from magnetic and electric field observations and are typically parameterised by electron drift shell (L^*) and geomagnetic indices (e.g. Kp index) (Ali et al., 2016; Ozeke et al., 2014; Murphy et al., 2023). Alternatively, event-specific diffusion coefficients can be useful for generating radiation belt simulations of specific storm events (Olifer et al., 2019), where estimated diffusion coefficients are not well-represented by empirical models with high variance (Ali et al., 2016; Sandhu, Rae, Wygant, et al., 2021). For these event-specific D_{LL}, ULF wave power in the magnetic and electric fields can be determined from one or multiple observation points (in situ or ground based) over a range of electron drift paths. However, radial diffusion treats the particle dynamics as a drift averaged process, so the D_{LL} estimate should represent the drift-averaged wave power that a given electron would experience along it's full drift orbit.

The presence of plumes and the results shown here raises some key questions regarding radial diffusion. Empirical models of D_{LL} assume comparable conditions at a given geomagnetic activity level (i.e. a given value of Kp for example). However, for some of these events there may be a plume contributing significant azimuthal asymmetry to the ULF wave power distribution. Event-specific diffusion coefficients often assume that the wave power observed at a given MLT is representative of the average wave power along the electron drift path. In this case, a localised enhancement in ULF wave power due to a plume would violate this assumption.

To establish how important plumes may be for radial diffusion processes and whether the contribution of spatially localised enhancements in ULF wave power are significant, we estimate event-specific D_{LL}s for these four events. We obtain radial diffusion coefficients for the magnetic field, $D^{\mathrm{B}}_{\mathrm{LL}}$, and the electric field, $D^{\mathrm{E}}_{\mathrm{LL}}$. The results are shown in Figure 6, and we refer the reader to the Supporting Information (S2) for full details on the calculations. Each column corresponds to each event, as labelled. Panels (a,c,e,g) show magnetic field diffusion coefficients, and panels (b,d,f,h) show the electric field counterpart. Each panel shows the diffusion coefficient as a function of L*, where L* is the third adiabatic invariant and can be considered as the radial measure of the electron drift orbit (Roederer, 1970; Roederer & Lejosne, 2018). We also include the empirically modelled diffusion coefficients by Ozeke et al. (2014), as shown by the black lines for comparison. We use the average Kp index value during this interval in the empirical model. The L* and Kp values used are shown in Table 1.

For each event, we identify the regions of enhanced and low ULF wave power, where the time intervals corresponding to the regions are shown in Table 1. For each region, the magnetic and electric field observations are used to estimate corresponding values of $D^{\mathbf{B}}_{\mathbf{LL}}$ and $D^{\mathbf{E}}_{\mathbf{LL}}$ (see Supporting Information S2). The $D_{\mathbf{LL}}$ values for the high power region are indicated by the rose asterisks, and the $D_{\mathbf{LL}}$ values for the low power region are indicated the indigo asterisks. For Events B, C, and D, we are able to reasonably estimate the azimuthal extent of the power enhancement from the timeseries, with the width in MLT shown in Table 1. Using the wave power inside, $P_{\mathbf{inside}}$ a plume of MLT width, $\mathbf{\Delta MLT}$, and outside the plume $P_{\mathbf{outside}}$, we can roughly estimate the drift averaged wave power along a drift path at the given L* as $\frac{P_{\mathbf{inside}}\mathbf{\Delta MLT}+P_{\mathbf{outside}}\mathbf{(24-\Delta MLT)}}{24}$. This assumes that $P_{\mathbf{outside}}$ is representative of the remainder of the drift path, but it is a reasonable assumption for these approximate first estimations. Using the drift-averaged wave power and the approach detailed in S2 of the Supporting Information, we estimate a more accurate MLT-averaged radial diffusion coefficient for the magnetic and electric components, which are indicated by the green asterisks in Figure 6. These MLT-averaged radial diffusion coefficients estimate the level of radial diffusion for an electron that experiences the plume (and spatially localised ULF wave power enhancement) along part of its orbit.

We briefly summarise key observations from the $D_{\mathbf{LL}}$ calculations below.

4.1.1 Event A

Figure 6a,b shows the radial diffusion coefficients estimated using the spacecraft ULF wave observations during the enhanced region (outside the plume, rose) and outside the enhancement (in the plume, indigo). We can see that there is a significant discrepancy between the rose and indigo asterisks, with the diffusion coefficients outside the plume observed over 2 orders of magnitude larger than the diffusion coefficients inside the plume. Whereas the observation inside the plume (indigo) is similar to the empirical model (black line) and thus representative of typical ULF wave power for these conditions, the diffusion coefficient outside the plume (rose) is higher than average. It ap-

Table 1. Table shows the parameters used for the radial diffusion coefficient calculations for each event.

Event	High Power Interval [UT]	Low Power Interval [UT]	MLT Width [h]	L*	Kp Index
A	16:20 - 16:30	15:30 - 15:40	-	4.75	3
B	00:00 - 03:00	23:00 - 23:30	2.9	4.25	6
C	14:20 - 15:20	15:30 - 15:40	0.6	4.75	3
D	03:35 - 04:45	05:00 - 05:10	0.7	4.5	3.3

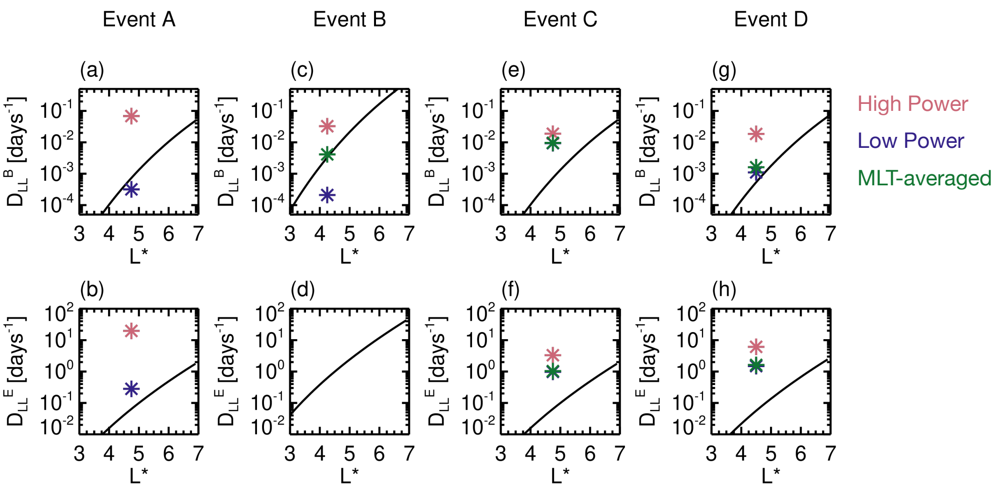

Figure 6. Radial diffusion coefficients as a function of L*. Each column corresponds to each event, as labelled. Panels (a,c,e,g) show the magnetic radial diffusion coefficient, $D_{\mathrm{LL}}^{\mathrm{B}}$ [days^{-1}], panels (b,d,f,h) show the electric radial diffusion coefficient, $D_{\mathrm{LL}}^{\mathrm{E}}$ [days^{-1}]. The solid black lines correspond to the Ozeke et al. (2014) modelled diffusion coefficients. The rose and indigo asterisks indicate the estimated diffusion coefficients for the high power and low power intervals (see Table 1). The green asterisks estimate the MLT-averaged radial diffusion coefficient.

pears that the empirical model is not capturing the magnitude of the solar wind driven ULF wave enhancement for this event. The general trend shown by the Ozeke et al. (2014) model also indicates that the majority of the difference is unlikely to be attributed to any difference in the L* value of the observations. We see similar trends for both the magnetic and electric field diffusion coefficients.

4.1.2 Event B

For this event there is a lack of electric field observations (Figure 3j,k), so we are restricted to analysis of only the magnetic field power and diffusion coefficients. Figure 6c shows that there is a notable difference between all three $D_{\mathbf{LL}}$ values, spanning almost 3 orders of magnitude in total. Reassuringly, the MLT-averaged coefficient lies very close to the Ozeke et al. (2014) model values (black line), suggesting that for this event the empirical model is capturing the magnitude of radial diffusion in the presence of a plume well. If a event-specific single spacecraft estimate of $D_{\mathbf{LL}}^{\mathbf{B}}$ was used for this event, the value would be significantly mis-representative. It could underestimate/overestimate $D_{\mathrm{LL}}^{\mathbf{B}}$ if it was outside/inside the plume by approximately an order of magnitude. Overall, the combination of a broad plume and large relative enhancement of wave power inside the plume result in a considerable impact on radial diffusion.

4.1.3 Event C

Figure 6e,f shows the estimated event-specific diffusion coefficients for these events, noting that the indigo asterisks is masked by the green asterisk (discussed in the next paragraph) in the same location. The values inside and outside of the plume are very similar, with less than an order of magnitude difference for both the magnetic and electric radial diffusion coefficients. Unsurprisingly, the relatively narrow plume width of less than 1 hour of MLT (see Table 1) has little impact on the MLT-averaged radial diffusion coefficient, such that the indigo and green asterisks overlap for both magnetic and electric field diffusion coefficients. For this case, the plume will have minimal impact on estimates of radial diffusion coefficients and on the radial diffusion experienced by the radiation belt electrons. We note that all event-specific estimates are larger than the Ozeke et al. (2014) modelled values by more than an order of magnitude for both the magnetic and electric field diffusion coefficients. We attribute this to the large variability in values that can be observed at a given activity level (Sandhu, Rae, Wygant, et al., 2021; Ali et al., 2016).

4.1.4 Event D

Figure 6g,h shows similar trends are observed for both the magnetic and electric diffusion coefficients, with the event-specific estimates larger than the Ozeke et al. (2014) empirical model for this event. The coefficients corresponding to the enhanced region (rose asterisks) are larger than the low power region (indigo asterisks) as expected, with a difference of more than one magnitude for the magnetic component. Figure 6g,h shows that the MLT-averaged diffusion coefficient and the low power coefficient (indigo and green) are very similar, such that the asterisks are almost completely overlapping. We deduce that, for this event, the relatively limited spatial extent of the enhanced region (less than 1 hour in MLT; Table 1) was insufficient to significantly contribute or alter the drift averaged wave power and hence enhance the radial diffusion coefficients.

Overall, Figure 6 demonstrates that event-specific diffusion coefficients inside a high power region can be largely unrepresentative of the MLT-averaged radial diffusion coefficient, and it is not accurate to assume that the observation of ULF wave power is representative of the electron drift path during during geomagnetic storms. The magnitude of the mis-estimation that can occur varies from event to event, depending on the nature of the ULF wave - plasma coupling. For example, Event B shows differences reaching multiple orders of magnitude. We recommend that event-specific diffusion coefficients should always take into account the background cold plasma density distribution, and utilise multi-spacecraft measurements to distinguish between spatially localised enhancements and global enhancements that would occur across a broader portion of an electron drift path.

Although current empirical models (Murphy et al., 2023)) are highly capable at capturing broad trends in $D_{\mathbf{LL}}$ with L*, solar wind conditions, and geomagnetic activity, there remains considerable model-observation error in $D_{\mathbf{LL}}$ at times. For example, Figure 4 of Murphy et al. (2023) shows that the model uncertainty can range over multiple orders of magnitude. We suggest here that a key source of model uncertainty can be attributed to the complex cold plasma - ULF wave coupling, which remains to be explicitly included in current radial diffusion models. To fully resolve this uncertainty, it is essential for further work to understand the role of plumes (and the cold plasma population in general), and this is a focus of future endeavours. We need to establish the physical properties that are missing from our theoretical understanding of radial transport and incorporate these factors into global models.

5 Concluding Thoughts

This report has presented a multiple event study analyses to highlight the complex and variable nature of ULF wave and cold plasma coupling during geomagnetic storms. The results demonstrate a clear need to understand the cold plasma and its structure during these dynamic periods. Although models such as Goldstein et al. (2019) and James et al. (2021) are highly capable at capturing the occurrence and shape of plumes, our results indicate that the gradients along plume edges are also important and need to be considered when modelling cold plasma density. The event studies also show that there are prominent knowledge gaps in how ULF wave generation and propagation are determined by plumes. The variability shows that the physical processes are highly sensitive to plume size and shape, as well as ULF wave driver characteristics.

We explored possible implications for radial diffusion and estimates of radial diffusion coefficients. The results indicate serious limitations with single spacecraft estimates and unrealistic $D_{\mathbf{LL}}$ calculations if plumes are unaccounted for. In particular, analysis suggests that plume contributions are specifically important for azimuthally broad structures that span a considerable MLT width, where trapped power within the plume can enhance $D_{\mathbf{LL}}$ values by more than an order of magnitude. These plumes are common in the early formation stages during geomagnetic storm main phase (Goldstein et al., 2004).

The results presented here highlight the need to realistically establish how radial transport manifests in the dynamic storm time inner magnetosphere, where electron drift paths intersect with plume structures. The analysis presented estimates of radial diffusion coefficients based on the average ULF wave power encountered along a complete electron drift orbit. However, these calculations are limited by existing derivations of radial diffusion coefficients that do not account for the presence of highly localised regions of enhanced power as observed here, and as such these average $D_{\mathbf{LL}}$ values should be strictly treated as simplistic estimates that are restricted by current best knowledge. Future progress in understanding ULF wave driven radial transport in the presence of plumes could include new theoretical derivations of radial diffusion coefficients and MHD simulations (e.g., A. Degeling et al., 2007). This work will include exploring how wave power is distributed across azimuthal wave numbers. For example, A. Degeling et al. (2007) shows that localised waves implies a spectrum of wave numbers (where each wave number relates to a drift resonant interaction with electrons with a specific drift speed), and hence the presence of multiple wave numbers is an important consideration in fully comprehending how ULF waves shape radial transport of electrons.

More broadly, there is evidence that other radiation belt model inputs may suffer from unrealistic inputs during storm times in addition to inaccuracies in radial diffusion inputs. For example, plumes have been observed to locally amplify and trap whistler mode waves (Shi et al., 2019; Ke et al., 2021), modify the chorus to hiss mechanism (Hartley et al., 2022), and are associated with enhanced EMIC wave activity (Usanova et al., 2013).

6 Open Research

Van Allen Probes and Sym H data is available from Coordinated Data Analysis Web (*Coordinated Data Analysis Web (CDAWeb) [dataset]*, n.d.). The solar wind data is publicly available from NASA/GSFC's Space Physics Data Facility's OMNIWeb service (Papitashvili & King, 2020). The Van Allen Probes plume crossing list is provided by Hartley (2022).

Acknowledgments

JKS acknowledges support from STFC grant ST/W00089X/1.
KRM and IJR acknowledge support from NERC grant NE/V002554/2 and STFC grants ST/V006320/1, ST/X001008/1.

Support for A.O. was provided by the Academy of Finland profiling action Matter and Materials (grant No. 318913).
DPH acknowledges NASA grant 80NSSC20K1324.
The contributions of JKS, IJR, and AWD were facilitated by the International Space Science Institute (ISSI) in Bern, through ISSI International Team project 483 (The Identification And Classification Of 3D Alfvén Resonances).
The scientific colour map batlow (Crameri, 2023) is used in this study to prevent visual distortion of the data and exclusion of readers with colour-vision deficiencies (Crameri et al., 2020).

References

Abe, S., Kawano, H., Goldstein, J., Ohtani, S., Solovyev, S. I., Baishev, D. G., & Yumoto, K. (2006). Simultaneous identification of a plasmaspheric plume by a ground magnetometer pair and image extreme ultraviolet imager. *Journal of Geophysical Research: Space Physics*, *111*(A11). Retrieved from `https://agupubs.onlinelibrary.wiley.com/doi/abs/10.1029/2006JA011653` doi: https://doi.org/10.1029/2006JA011653

Ali, A. F., Malaspina, D. M., Elkington, S. R., Jaynes, A. N., Chan, A. A., Wygant, J., & Kletzing, C. A. (2016). Electric and magnetic radial diffusion coefficients using the van allen probes data. *Journal of Geophysical Research: Space Physics*, *121*(10), 9586-9607. Retrieved from `https://agupubs.onlinelibrary.wiley.com/doi/abs/10.1002/2016JA023002` doi: https://doi.org/10.1002/2016JA023002

Blake, J. B., Carranza, P. A., Claudepierre, S. G., Clemmons, J. H., Crain, W. R., Dotan, Y., … Zakrzewski, M. P. (2013). The magnetic electron ion spectrometer (mageis) instruments aboard the radiation belt storm probes (rbsp) spacecraft. *Space Science Reviews*, *179*(1), 383–421.

Borovsky, J. E., & Denton, M. H. (2008). A statistical look at plasmaspheric drainage plumes. *Journal of Geophysical Research: Space Physics*, *113*(A9). Retrieved from `https://agupubs.onlinelibrary.wiley.com/doi/abs/10.1029/2007JA012994` doi: https://doi.org/10.1029/2007JA012994

Breneman, A. W., Wygant, J. R., Tian, S., Cattell, C. A., Thaller, S. A., Goetz, K., … Halford, A. J. (2022). The van allen probes electric field and waves instrument: Science results, measurements, and access to data. *Space Science Reviews*, *218*(8), 69.

Chen, A., & Wolf, R. (1972). Effects on the plasmasphere of a time-varying convection electric field. *Planetary and Space Science*, *20*(4), 483-509. Retrieved from `https://www.sciencedirect.com/science/article/pii/0032063372900803` doi: https://doi.org/10.1016/0032-0633(72)90080-3

Coordinated data analysis web (cdaweb) [dataset]. (n.d.). `https://cdaweb.gsfc.nasa.gov`. (Accessed: 14/11/2023)

Crameri, F. (2023, October). *Scientific colour maps.* Zenodo. Retrieved from `https://doi.org/10.5281/zenodo.8409685` doi: 10.5281/zenodo.8409685

Crameri, F., Shephard, G. E., & Heron, P. J. (2020). The misuse of colour in science communication. *Nature Communications*, *11*(1), 5444.

Darrouzet, F., De Keyser, J., Décréau, P. M. E., El Lemdani-Mazouz, F., & Vallières, X. (2008). Statistical analysis of plasmaspheric plumes with cluster/whisper observations. *Annales Geophysicae*, *26*(8), 2403–2417. Retrieved from `https://angeo.copernicus.org/articles/26/2403/2008/` doi: 10.5194/angeo-26-2403-2008

Darrouzet, F., Gallagher, D. L., André, N., Carpenter, D. L., Dandouras, I., Décréau, P. M. E., … Tu, J. (2009). Plasmaspheric density structures and dynamics: Properties observed by the cluster and image missions. *Space Science Reviews*, *145*(1), 55–106.

Degeling, A., Rankin, R., Kabin, K., Marchand, R., & Mann, I. (2007). The effect of ulf compressional modes and field line resonances on relativistic electron dynamics. *Planetary and Space Science*, *55*(6), 731-742. Retrieved from https://www.sciencedirect.com/science/article/pii/S0032063306002893 (Ultra-Low Frequency Waves in the Magnetosphere) doi: https://doi.org/10.1016/j.pss.2006.04.039

Degeling, A. W., Ozeke, L. G., Rankin, R., Mann, I. R., & Kabin, K. (2008). Drift resonant generation of peaked relativistic electron distributions by pc 5 ulf waves. *Journal of Geophysical Research: Space Physics*, *113*(A2). Retrieved from https://agupubs.onlinelibrary.wiley.com/doi/abs/10.1029/2007JA012411 doi: https://doi.org/10.1029/2007JA012411

Degeling, A. W., Rae, I. J., Watt, C. E. J., Shi, Q. Q., Rankin, R., & Zong, Q.-G. (2018). Control of ulf wave accessibility to the inner magnetosphere by the convection of plasma density. *Journal of Geophysical Research: Space Physics*, *123*(2), 1086-1099. Retrieved from https://agupubs.onlinelibrary.wiley.com/doi/abs/10.1002/2017JA024874 doi: 10.1002/2017JA024874

Dungey, J. W. (1954). Electrodynamics of the outer atmosphere. *Pennsylvania State University Ionosphere Research Laboratory Science Report*, *69*.

Elkington, S. R., Hudson, M. K., & Chan, A. A. (2003). Resonant acceleration and diffusion of outer zone electrons in an asymmetric geomagnetic field. *Journal of Geophysical Research: Space Physics*, *108*(A3). Retrieved from https://agupubs.onlinelibrary.wiley.com/doi/abs/10.1029/2001JA009202 doi: 10.1029/2001JA009202

Elsden, T., Wright, A., & Degeling, A. (2022). A review of the theory of 3-d alfvén (field line) resonances. *Frontiers in Astronomy and Space Sciences*, *9*. Retrieved from https://www.frontiersin.org/articles/10.3389/fspas.2022.917817 doi: 10.3389/fspas.2022.917817

Elsden, T., & Wright, A. N. (2022). Polarization properties of 3-d field line resonances. *Journal of Geophysical Research: Space Physics*, *127*(2), e2021JA030080. Retrieved from https://agupubs.onlinelibrary.wiley.com/doi/abs/10.1029/2021JA030080 (e2021JA030080 2021JA030080) doi: https://doi.org/10.1029/2021JA030080

Elsden, T., Yeoman, T. K., Wharton, S. J., Rae, I. J., Sandhu, J. K., Walach, M.-T., ... Wright, D. M. (2022). Modeling the varying location of field line resonances during geomagnetic storms. *Journal of Geophysical Research: Space Physics*, *127*(1), e2021JA029804. Retrieved from https://agupubs.onlinelibrary.wiley.com/doi/abs/10.1029/2021JA029804 (e2021JA029804 2021JA029804) doi: https://doi.org/10.1029/2021JA029804

Forsyth, C., Rae, I. J., Coxon, J. C., Freeman, M. P., Jackman, C. M., Gjerloev, J., & Fazakerley, A. N. (2015). A new technique for determining substorm onsets and phases from indices of the electrojet (sophie). *Journal of Geophysical Research: Space Physics*, *120*(12), 10,592-10,606. Retrieved from https://agupubs.onlinelibrary.wiley.com/doi/abs/10.1002/2015JA021343 doi: https://doi.org/10.1002/2015JA021343

Fälthammar, C.-G. (1965). Effects of time-dependent electric fields on geomagnetically trapped radiation. *Journal of Geophysical Research (1896-1977)*, *70*(11), 2503-2516. Retrieved from https://agupubs.onlinelibrary.wiley.com/doi/abs/10.1029/JZ070i011p02503 doi: 10.1029/JZ070i011p02503

George, H., Reeves, G., Cunningham, G., Kalliokoski, M. M. H., Kilpua, E., Osmane, A., ... Palmroth, M. (2022). Contributions to loss across the magnetopause during an electron dropout event. *Journal of Geophysical Research: Space Physics*, *127*(10), e2022JA030751. Retrieved from https://agupubs.onlinelibrary.wiley.com/doi/abs/10.1029/2022JA030751 (e2022JA030751 2022JA030751) doi: https://doi.org/10.1029/2022JA030751

Goldstein, J., Pascuale, S., & Kurth, W. S. (2019). Epoch-based model for storm-time plasmapause location. *Journal of Geophysical Research: Space Physics*, *124*(6), 4462-4491. Retrieved from `https://agupubs.onlinelibrary.wiley.com/doi/abs/10.1029/2018JA025996` doi: https://doi.org/10.1029/2018JA025996

Goldstein, J., Pascuale, S. D., Kletzing, C., Kurth, W., Genestreti, K. J., Skoug, R. M., … Spence, H. (2014). Simulation of van allen probes plasmapause encounters. *Journal of Geophysical Research: Space Physics*, *119*(9), 7464-7484. Retrieved from `https://agupubs.onlinelibrary.wiley.com/doi/abs/10.1002/2014JA020252` doi: https://doi.org/10.1002/2014JA020252

Goldstein, J., Sandel, B. R., Thomsen, M. F., Spasojević, M., & Reiff, P. H. (2004). Simultaneous remote sensing and in situ observations of plasmaspheric drainage plumes. *Journal of Geophysical Research: Space Physics*, *109*(A3). Retrieved from `https://agupubs.onlinelibrary.wiley.com/doi/abs/10.1029/2003JA010281` doi: https://doi.org/10.1029/2003JA010281

Hao, Y. X., Zong, Q.-G., Zhou, X.-Z., Rankin, R., Chen, X. R., Liu, Y., … Claudepierre, S. G. (2019). Global-scale ulf waves associated with ssc accelerate magnetospheric ultrarelativistic electrons. *Journal of Geophysical Research: Space Physics*, *124*(3), 1525-1538. Retrieved from `https://agupubs.onlinelibrary.wiley.com/doi/abs/10.1029/2018JA026134` doi: https://doi.org/10.1029/2018JA026134

Hartley, D. P. (2022). *List of plasmaspheric plumes from van allen probes (rbsp) [dataset].* University of Iowa. doi: https://doi.org/10.25820/data.006173

Hartley, D. P., Chen, L., Christopher, I. W., Kletzing, C. A., Santolik, O., Li, W., & Shi, R. (2022). The angular distribution of lower band chorus waves near plasmaspheric plumes. *Geophysical Research Letters*, *49*(9), e2022GL098710. Retrieved from `https://agupubs.onlinelibrary.wiley.com/doi/abs/10.1029/2022GL098710` (e2022GL098710 2022GL098710) doi: https://doi.org/10.1029/2022GL098710

Hutchinson, J. A., Wright, D. M., & Milan, S. E. (2011). Geomagnetic storms over the last solar cycle: A superposed epoch analysis. *Journal of Geophysical Research: Space Physics*, *116*(A9). Retrieved from `https://agupubs.onlinelibrary.wiley.com/doi/abs/10.1029/2011JA016463` doi: https://doi.org/10.1029/2011JA016463

Iyemori, T. (1990). Storm-time magnetospheric currents inferred from mid-latitude geomagnetic field variations. *Journal of Geomagnetism and Geoelectricity*, *42*, 1249-1265.

Jacobs, J. A., Kato, Y., Matsushita, S., & Troitskaya, V. A. (1964). Classification of geomagnetic micropulsations. *Journal of Geophysical Research (1896-1977)*, *69*(1), 180-181. Retrieved from `https://agupubs.onlinelibrary.wiley.com/doi/abs/10.1029/JZ069i001p00180` doi: https://doi.org/10.1029/JZ069i001p00180

James, M. K., Yeoman, T. K., Jones, P., Sandhu, J. K., & Goldstein, J. (2021). The scalable plasma ion composition and electron density (spiced) model for earth's inner magnetosphere. *Journal of Geophysical Research: Space Physics*, *126*(9), e2021JA029565. Retrieved from `https://agupubs.onlinelibrary.wiley.com/doi/abs/10.1029/2021JA029565` (e2021JA029565 2021JA029565) doi: https://doi.org/10.1029/2021JA029565

James, M. K., Yeoman, T. K., Mager, P. N., & Klimushkin, D. Y. (2013). The spatio-temporal characteristics of ulf waves driven by substorm injected particles. *Journal of Geophysical Research: Space Physics*, *118*(4), 1737-1749. Retrieved from `https://agupubs.onlinelibrary.wiley.com/doi/abs/10.1002/jgra.50131` doi: 10.1002/jgra.50131

Jaynes, A. N., Ali, A. F., Elkington, S. R., Malaspina, D. M., Baker, D. N., Li, X., … Wygant, J. R. (2018). Fast diffusion of ultrarelativistic electrons in the outer radiation belt: 17 march 2015 storm event. *Geophysical Research Letters*, *45*(20), 10,874-10,882. Retrieved from https://agupubs.onlinelibrary.wiley.com/doi/abs/10.1029/2018GL079786 doi: https://doi.org/10.1029/2018GL079786

Katsavrias, C., Daglis, I. A., & Li, W. (2019). On the statistics of acceleration and loss of relativistic electrons in the outer radiation belt: A superposed epoch analysis. *Journal of Geophysical Research: Space Physics*, *124*(4), 2755-2768. Retrieved from https://agupubs.onlinelibrary.wiley.com/doi/abs/10.1029/2019JA026569 doi: https://doi.org/10.1029/2019JA026569

Ke, Y., Chen, L., Gao, X., Lu, Q., Wang, X., Chen, R., … Wang, S. (2021). Whistler-mode waves trapped by density irregularities in the earth's magnetosphere. *Geophysical Research Letters*, *48*(7), e2020GL092305. Retrieved from https://agupubs.onlinelibrary.wiley.com/doi/abs/10.1029/2020GL092305 (e2020GL092305 2020GL092305) doi: https://doi.org/10.1029/2020GL092305

Kellogg, P. J. (1959). Van allen radiation of solar origin. *Nature*, *183*(4671), 1295–1297.

Kivelson, M. G., & Southwood, D. J. (1986). Coupling of global magnetospheric mhd eigenmodes to field line resonances. *Journal of Geophysical Research: Space Physics*, *91*(A4), 4345-4351. Retrieved from https://agupubs.onlinelibrary.wiley.com/doi/abs/10.1029/JA091iA04p04345 doi: https://doi.org/10.1029/JA091iA04p04345

Kletzing, C. A., Bortnik, J., Hospodarsky, G., Kurth, W. S., Santolik, O., Smitth, C. W., … Sen Gupta, A. (2023). The electric and magnetic fields instrument suite and integrated science (emfisis): Science, data, and usage best practices. *Space Science Reviews*, *219*(4), 28.

Kletzing, C. A., Kurth, W. S., Acuna, M., MacDowall, R. J., Torbert, R. B., Averkamp, T., … Tyler, J. (2013, Nov 01). The Electric and Magnetic Field Instrument Suite and Integrated Science (EMFISIS) on RBSP. *Space Science Reviews*, *179*(1), 127–181. Retrieved from https://doi.org/10.1007/s11214-013-9993-6 doi: 10.1007/s11214-013-9993-6

Kurth, W. S., De Pascuale, S., Faden, J. B., Kletzing, C. A., Hospodarsky, G. B., Thaller, S., & Wygant, J. R. (2015). Electron densities inferred from plasma wave spectra obtained by the waves instrument on van allen probes. *Journal of Geophysical Research: Space Physics*, *120*(2), 904-914. Retrieved from https://agupubs.onlinelibrary.wiley.com/doi/abs/10.1002/2014JA020857 doi: https://doi.org/10.1002/2014JA020857

Lee, D.-H., Hudson, M. K., Kim, K., Lysak, R. L., & Song, Y. (2002). Compressional mhd wave transport in the magnetosphere 1. reflection and transmission across the plasmapause. *Journal of Geophysical Research: Space Physics*, *107*(A10), SMP 16-1-SMP 16-14. Retrieved from https://agupubs.onlinelibrary.wiley.com/doi/abs/10.1029/2002JA009239 doi: 10.1029/2002JA009239

Lejosne, S., & Kollmann, P. (2020). Radiation belt radial diffusion at earth and beyond. *Space Science Reviews*, *216*(1), 19.

Moldwin, M. B., Thomsen, M. F., Bame, S. J., McComas, D. J., & Moore, K. R. (1994). An examination of the structure and dynamics of the outer plasmasphere using multiple geosynchronous satellites. *Journal of Geophysical Research: Space Physics*, *99*(A6), 11475-11481. Retrieved from https://agupubs.onlinelibrary.wiley.com/doi/abs/10.1029/93JA03526 doi: https://doi.org/10.1029/93JA03526

Murphy, K. R., Sandhu, J. K., Rae, I. J., Daggitt, T. A., Glauert, S. A., Horne, R. B., … Wygant, J. (2023, feb). A new four-component l∗-dependent model for radial diffusion based on solar wind and magnetospheric drivers of ULF waves. *ESSOAR*. Retrieved from https://doi.org/10.22541/essoar

.167591092.27672309/v1 doi: 10.22541/essoar.167591092.27672309/v1

Newell, P. T., & Gjerloev, J. W. (2011). Evaluation of supermag auroral electrojet indices as indicators of substorms and auroral power. *Journal of Geophysical Research: Space Physics*, *116*(A12). Retrieved from https://agupubs.onlinelibrary.wiley.com/doi/abs/10.1029/2011JA016779 doi: https://doi.org/10.1029/2011JA016779

Olifer, L., Mann, I. R., Ozeke, L. G., Rae, I. J., & Morley, S. K. (2019). On the relative strength of electric and magnetic ulf wave radial diffusion during the march 2015 geomagnetic storm. *Journal of Geophysical Research: Space Physics*, *124*(4), 2569-2587. Retrieved from https://agupubs.onlinelibrary.wiley.com/doi/abs/10.1029/2018JA026348 doi: https://doi.org/10.1029/2018JA026348

Osmane, A., Kilpua, E., George, H., Allanson, O., & Kalliokoski, M. (2023). Radial transport in the earth's radiation belts: Linear, quasi-linear, and higher-order processes. *The Astrophysical Journal Supplement Series*, *269*(2), 44.

Ozeke, L. G., Mann, I. R., Murphy, K. R., Rae, I. J., & Milling, D. K. (2014). Analytic expressions for ulf wave radiation belt radial diffusion coefficients. *Journal of Geophysical Research: Space Physics*, *119*(3), 1587-1605. Retrieved from https://agupubs.onlinelibrary.wiley.com/doi/abs/10.1002/2013JA019204 doi: https://doi.org/10.1002/2013JA019204

Papitashvili, N. E., & King, J. H. (2020). *Omni 1-min data set [dataset].* NASA Space Physics Data Facility. doi: https://doi.org/10.48322/45bb-8792

Parker, E. N. (1960). Geomagnetic fluctuations and the form of the outer zone of the van allen radiation belt. *Journal of Geophysical Research (1896-1977)*, *65*(10), 3117-3130. Retrieved from https://agupubs.onlinelibrary.wiley.com/doi/abs/10.1029/JZ065i010p03117 doi: 10.1029/JZ065i010p03117

Rae, I. J., Murphy, K. R., Watt, C. E., Sandhu, J. K., Georgiou, M., Degeling, A. W., ... Shi, Q. (2019). How do ultra-low frequency waves access the inner magnetosphere during geomagnetic storms? *Geophysical Research Letters*, *46*(19), 10699-10709. Retrieved from https://agupubs.onlinelibrary.wiley.com/doi/abs/10.1029/2019GL082395 doi: 10.1029/2019GL082395

Rae, I. J., Murphy, K. R., Watt, C. E. J., Halford, A. J., Mann, I. R., Ozeke, L. G., ... Singer, H. J. (2018). The role of localized compressional ultra-low frequency waves in energetic electron precipitation. *Journal of Geophysical Research: Space Physics*, *123*(3), 1900-1914. Retrieved from https://agupubs.onlinelibrary.wiley.com/doi/abs/10.1002/2017JA024674 doi: https://doi.org/10.1002/2017JA024674

Ren, J., Zong, Q.-G., Miyoshi, Y., Zhou, X. Z., Wang, Y. F., Rankin, R., ... Kletzing, C. A. (2017). Low-energy (¡200 ev) electron acceleration by ulf waves in the plasmaspheric boundary layer: Van allen probes observation. *Journal of Geophysical Research: Space Physics*, *122*(10), 9969-9982. Retrieved from https://agupubs.onlinelibrary.wiley.com/doi/abs/10.1002/2017JA024316 doi: https://doi.org/10.1002/2017JA024316

Roederer, J. G. (1970). *Dynamics of geomagnetically trapped radiation.* Springer, Berlin, Heidelberg.

Roederer, J. G., & Lejosne, S. (2018). Coordinates for representing radiation belt particle flux. *Journal of Geophysical Research: Space Physics*, *123*(2), 1381-1387. Retrieved from https://agupubs.onlinelibrary.wiley.com/doi/abs/10.1002/2017JA025053 doi: 10.1002/2017JA025053

Sandhu, J. K., Degeling, A. W., Elsden, T., Murphy, K. R., Rae, I. J., Wright, A. N., ... Smith, A. (2023). Van allen probes observations of a three-dimensional field line resonance at a plasmaspheric plume. *Geophysical Research Letters*, *50*(23), e2023GL106715. Retrieved from https://agupubs.onlinelibrary.wiley.com/doi/abs/10.1029/2023GL106715 (e2023GL106715 2023GL106715) doi: https://doi.org/10.1029/2023GL106715

Sandhu, J. K., Rae, I. J., Staples, F. A., Hartley, D. P., Walach, M.-T., Elsden, T., & Murphy, K. R. (2021). The roles of the magnetopause and plasmapause in storm-time ulf wave power enhancements. *Journal of Geophysical Research: Space Physics*, *126*(7), e2021JA029337. Retrieved from `https://agupubs.onlinelibrary.wiley.com/doi/abs/10.1029/2021JA029337` (e2021JA029337 2021JA029337) doi: https://doi.org/10.1029/2021JA029337

Sandhu, J. K., Rae, I. J., & Walach, M.-T. (2021). Challenging the use of ring current indices during geomagnetic storms. *Journal of Geophysical Research: Space Physics*, *126*(2), e2020JA028423. Retrieved from `https://agupubs.onlinelibrary.wiley.com/doi/abs/10.1029/2020JA028423` (e2020JA028423 2020JA028423) doi: https://doi.org/10.1029/2020JA028423

Sandhu, J. K., Rae, I. J., Wygant, J. R., Breneman, A. W., Tian, S., Watt, C. E. J., … Walach, M.-T. (2021). Ulf wave driven radial diffusion during geomagnetic storms: A statistical analysis of van allen probes observations. *Journal of Geophysical Research: Space Physics*, *126*(4), e2020JA029024. Retrieved from `https://agupubs.onlinelibrary.wiley.com/doi/abs/10.1029/2020JA029024` (e2020JA029024 2020JA029024) doi: https://doi.org/10.1029/2020JA029024

Sandhu, J. K., Yeoman, T. K., James, M. K., Rae, I. J., & Fear, R. C. (2018). Variations of high-latitude geomagnetic pulsation frequencies: A comparison of time-of-flight estimates and image magnetometer observations. *Journal of Geophysical Research: Space Physics*, *123*(1), 567-586. Retrieved from `https://agupubs.onlinelibrary.wiley.com/doi/abs/10.1002/2017JA024434` doi: https://doi.org/10.1002/2017JA024434

Sandhu, J. K., Yeoman, T. K., & Rae, I. J. (2018). Variations of field line eigenfrequencies with ring current intensity. *Journal of Geophysical Research: Space Physics*, *123*(11), 9325-9339. Retrieved from `https://agupubs.onlinelibrary.wiley.com/doi/abs/10.1029/2018JA025751` doi: 10.1029/2018JA025751

Sandhu, J. K., Yeoman, T. K., Rae, I. J., Fear, R. C., & Dandouras, I. (2017). The dependence of magnetospheric plasma mass loading on geomagnetic activity using cluster. *Journal of Geophysical Research: Space Physics*, *122*(9), 9371-9395. Retrieved from `https://agupubs.onlinelibrary.wiley.com/doi/abs/10.1002/2017JA024171` doi: 10.1002/2017JA024171

Shi, R., Li, W., Ma, Q., Green, A., Kletzing, C. A., Kurth, W. S., … Reeves, G. D. (2019). Properties of whistler mode waves in earth's plasmasphere and plumes. *Journal of Geophysical Research: Space Physics*, *124*(2), 1035-1051. Retrieved from `https://agupubs.onlinelibrary.wiley.com/doi/abs/10.1029/2018JA026041` doi: https://doi.org/10.1029/2018JA026041

Smith, A. W., Rae, I. J., Forsyth, C., Watt, C. E. J., & Murphy, K. R. (2023). Statistical characterisation of the dynamic near-earth plasma sheet relative to ultra-low frequency (ulf) wave growth at substorm onset. *Journal of Geophysical Research: Space Physics*, *n/a*(n/a), e2022JA030491. Retrieved from `https://agupubs.onlinelibrary.wiley.com/doi/abs/10.1029/2022JA030491` (e2022JA030491 2022JA030491) doi: https://doi.org/10.1029/2022JA030491

Southwood, D. (1974). Some features of field line resonances in the magnetosphere. *Planetary and Space Science*, *22*(3), 483 - 491. Retrieved from `http://www.sciencedirect.com/science/article/pii/0032063374900786` doi: https://doi.org/10.1016/0032-0633(74)90078-6

Staples, F. A., Kellerman, A., Murphy, K. R., Rae, I. J., Sandhu, J. K., & Forsyth, C. (2022). Resolving magnetopause shadowing using multimission measurements of phase space density. *Journal of Geophysical Research: Space Physics*, *127*(2), e2021JA029298. Retrieved from `https://agupubs.onlinelibrary.wiley.com/doi/abs/10.1029/2021JA029298`

(e2021JA029298 2021JA029298) doi: https://doi.org/10.1029/2021JA029298
Turner, D. L., Shprits, Y., Hartinger, M., & Angelopoulos, V. (2012). Explaining sudden losses of outer radiation belt electrons during geomagnetic storms. *Nature Physics*, *8*(3), 208–212.
Usanova, M. E., Darrouzet, F., Mann, I. R., & Bortnik, J. (2013). Statistical analysis of emic waves in plasmaspheric plumes from cluster observations. *Journal of Geophysical Research: Space Physics*, *118*(8), 4946-4951. Retrieved from https://agupubs.onlinelibrary.wiley.com/doi/abs/10.1002/jgra.50464 doi: https://doi.org/10.1002/jgra.50464
Walach, M.-T. (2023). *Geomagnetic storm list 1981-2019 [dataset].* Lancaster University. doi: https://doi.org/10.17635/lancaster/researchdata/622
Wharton, S. J., Rae, I. J., Sandhu, J. K., Walach, M.-T., Wright, D. M., & Yeoman, T. K. (2020). The changing eigenfrequency continuum during geomagnetic storms: Implications for plasma mass dynamics and ulf wave couping. *Journal of Geophysical Research: Space Physics*, *n/a*(n/a), e2019JA027648. Retrieved from https://agupubs.onlinelibrary.wiley.com/doi/abs/10.1029/2019JA027648 (e2019JA027648 2019JA027648) doi: 10.1029/2019JA027648
Wygant, J. R., Bonnell, J. W., Goetz, K., Ergun, R. E., Mozer, F. S., Bale, S. D., ... Tao, J. B. (2013). The electric field and waves instruments on the radiation belt storm probes mission. *Space Science Reviews*, *179*(1), 183–220.
Zhang, S., Tian, A., Degeling, A. W., Shi, Q., Wang, M., Hao, Y., ... Bai, S. (2019). Pc4-5 poloidal ulf wave observed in the dawnside plasmaspheric plume. *Journal of Geophysical Research: Space Physics*, *124*(12), 9986-9998. Retrieved from https://agupubs.onlinelibrary.wiley.com/doi/abs/10.1029/2019JA027319 doi: https://doi.org/10.1029/2019JA027319

Supporting Information for "The spatial localisation of storm-time ULF waves due to plasmaspheric plumes and implications for calculating radial diffusion"

J. K. Sandhu[1,2], K. R. Murphy[2], I. J. Rae[2], A. W. Degeling[3], A. Osmane[4],

D. P. Hartley[5], and L. Olifer[6]

[1]Department of Physics and Astronomy, University of Leicester, Leicester, UK

[2]Department of Maths, Physics and Electrical Engineering, Northumbria University, Newcastle Upon Tyne, UK

[3]Institute of Space Science, Shandong University, Weihai, China

[4]Department of Physics, University of Helsinki, Helsinki, Finland

[5]Department of Physics and Astronomy, University of Iowa, Iowa City, IA, USA

[6]Department of Physics, University of Alberta, Edmonton, AB, Canada

Contents of this file

1. Text S1 to S2

Introduction This Supporting Information provides further details on aspects of the main manuscript. S1 presents MAGEIS information providing evidence for a drift-resonant interaction between protons and the FLR observed in Event A. S2 includes full details

---

Corresponding author: J. K. Sandhu, Department of Physics and Astronomy, University of Leicester, Leicester, UK. (jasmine.sandhu@leicester.ac.uk)

on how the radial diffusion coefficients are calculated, using Event D as an illustrative example.

S1. MAGEIS Data Analysis for Event A

To assess whether the $\sim$ 10 mHz signature in the radial magnetic field component is associated with a drift-resonant driven poloidal FLR, we consulted MagEIS observations of energetic ring current protons. Figure S1a shows residual fluxes of 90 degree pitch angle protons at each energy channel, as a function of time. Residual flux, j, is defined as $\frac{j_i - j_0}{j_0}$, where j_i is the differential proton flux at a given time, energy bin, and pitch angle bin, and j_0 is the median flux value over a 10 minute window centred on the sample time and the identical energy and pitch angle bin. This definition of residual flux follows standard usage by (e.g., Claudepierre et al., 2013; Zhao et al., 2021). Each timeseries shown in Figure S1a is bandpass filtered for frequencies between 8 to 12 mHz to focus on frequencies similar to the $\sim$ 10 mHz magnetic field signature. We observe high amplitude periodic fluctuations in the 479 keV protons at $\sim$16:20 UT, with evidence for a phase change between the 479 and 555 keV energy channels (see the timeseries are in anti-phase with each other). Figure S1b shows the amplitude, A, and phase ϕ, of the timeseries for a 10 minute window centred on 16:17 UT. The profiles confirm a clear peak in amplitude accompanied by a $\sim$ 180 degree phase shift at $\sim$ 479 keV. These characteristic features are convincing evidence for drift resonance between the protons and the $\sim$ 10 mHz ULF wave (D. J. Southwood & Kivelson, 1981; Claudepierre et al., 2013).

We apply the drift resonance condition for a 10 mHz wave and a 479 keV proton (D. Southwood et al., 1969) (see Figure S1c). We estimate that the ULF wave has a wavenumber of approx -100 and is westward propagating, within the typical range of high-m substorm driven ULF waves (Takahashi et al., 1985; Murphy et al., 2018).

If the drift resonance is supporting a fundamental standing Alfvén wave, we can compare the 10 mHz pulsation to the estimated eigenfrequency of the local field line. Using a time-of-flight estimate with the TS04 magnetic field model, and local mass density measurements (EMFISIS electron density and HOPE ion composition (James et al., 2021; Sandhu et al., 2016, 2017)) we estimate the local eigenfrequencies (e.g., Sandhu et al., 2018, 2023). We estimate the fundamental eigenfrequency outside the plume is approximately 20 mHz and inside the plume it is decreased to approximately 4 mHz. The estimates show how the plume density dramatically alters the local eigenfrequency and is therefore capable to excluding the wave interaction from occurring and localises the FLR to the low density region (Zhang et al., 2019). We note that the calculated 20 mHz eigenfrequency is higher than the 10 mHz observed FLR. We attribute the difference to inaccuracies in our eigenfrequency estimates (e.g. choice of field model, assumed field-aligned mass density profile, ion composition estimates). It is outside of the scope to investigate these further, and we provide the eigenfrequency estimates as a approximate guide here.

S2. Estimating Radial Diffusion Coefficients

For a given frequency-resolved measurement of ULF wave power, we can estimate corresponding radial diffusion coefficients, assuming that the wave power value represents the average value across an electron drift orbit. We use the Ozeke, Mann, Murphy, Rae, and Milling (2014) formalism, which represents the magnetic field diffusion coefficient, $D_{\mathrm{LL}}^{\mathrm{B}}$, and the electric field diffusion coefficient, $D_{\mathrm{LL}}^{\mathrm{E}}$, by equations 1 and 2 below. B_E is the equatorial magnetic field strength at the surface of the Earth, R_E is the radius of the Earth, L is the L-shell, and f is frequency. We can substitute the observed power spectral density for the compressional magnetic field, P_{B}, and azimuthal electric field, P_{E}, into equations 1 and 2 to estimate event-specific diffusion coefficients.

$$D_{LL}^{B} = \frac{L^8 4\pi^2}{9 \times 8 B_E^2} \langle P^B(L,f) f^2 \rangle \tag{1}$$

$$D_{LL}^{E} = \frac{L^6}{8 B_E^2 R_E^2} \langle P^E(L,f) \rangle \tag{2}$$

We now detail how this approach is used to derive the diffusion coefficients presented in the main text. Using Event D as an illustrative example, Figure S2a shows the electron density timeseries through the plume crossing on 24 June 2015 (Event D; Figure 4. Panel (b) shows the timeseries for the total magnetic field power (wine) and total electric field wave power (green) summed over 1 - 15 mHz, and panel (c) shows the location of the spacecraft in L* (indigo) and MLT (rose). The L* value is calculated using the International Radiation Belt Environment Modeling (IRBEM) code (https://sourceforge.net/projects/irbem/) with the Tsyganenko and Sitnov (2005) magnetic field model for an equatorially trapped particle. Figure S2b shows the localised enhancement in magnetic and electric field wave power along the edge of the plume, as discussed in the main text. Note that the y-axis is logarithmic, such that changes are over several orders of magnitude. The width of the power enhancement is roughly estimated by eye and indicated by the grey shaded region in panels (a-d).

Figure S2d,e show the radial diffusion coefficients estimated using the spacecraft ULF wave observations during the enhanced region (rose) and outside the enhancement (indigo). The time intervals corresponding to the samples are shown in Table 1. The x-axis shows the L*, and the event-specific diffusion coefficients use the average L* value across the two samples. By estimating the width of the plume, we also show the MLT-averaged radial diffusion (green, see main text for details), where the green and indigo asterisks are almost completely colocated on panels (d,e). We note that we have been relatively conservative when visually identifying the enhanced regions for these events, such that the magnitudes of any differences are assumed to be towards the lower limit.

This approach was extended to all event studies, where the appropriate details are included in Table 1 in the main manuscript.

References

Claudepierre, S. G., Mann, I. R., Takahashi, K., Fennell, J. F., Hudson, M. K., Blake, J. B., ... Wygant, J. R. (2013). Van allen probes observation of localized drift resonance between poloidal mode ultra-low frequency waves and 60 kev electrons. *Geophysical Research Letters*, *40*(17), 4491-4497. Retrieved from `https://agupubs.onlinelibrary.wiley.com/doi/abs/10.1002/grl.50901` doi: https://doi.org/10.1002/grl.50901

James, M. K., Yeoman, T. K., Jones, P., Sandhu, J. K., & Goldstein, J. (2021). The scalable plasma ion composition and electron density (spiced) model for earth's inner magnetosphere. *Journal of Geophysical Research: Space Physics*, *126*(9), e2021JA029565. Retrieved from `https://agupubs.onlinelibrary.wiley.com/doi/abs/10.1029/2021JA029565` (e2021JA029565 2021JA029565) doi: https://doi.org/10.1029/2021JA029565

Murphy, K. R., Inglis, A. R., Sibeck, D. G., Rae, I. J., Watt, C. E. J., Silveira, M., ...

Nakamura, R. (2018). Determining the mode, frequency, and azimuthal wave number of ulf waves during a hss and moderate geomagnetic storm. *Journal of Geophysical Research: Space Physics*, *123*(8), 6457-6477. Retrieved from https://agupubs.onlinelibrary.wiley.com/doi/abs/10.1029/2017JA024877 doi: https://doi.org/10.1029/2017JA024877

Ozeke, L. G., Mann, I. R., Murphy, K. R., Rae, I. J., & Milling, D. K. (2014). Analytic expressions for ulf wave radiation belt radial diffusion coefficients. *Journal of Geophysical Research: Space Physics*, *119*(3), 1587-1605. Retrieved from https://agupubs.onlinelibrary.wiley.com/doi/abs/10.1002/2013JA019204 doi: https://doi.org/10.1002/2013JA019204

Sandhu, J. K., Degeling, A. W., Elsden, T., Murphy, K. R., Rae, I. J., Wright, A. N., ... Smith, A. (2023). Van allen probes observations of a three-dimensional field line resonance at a plasmaspheric plume. *Geophysical Research Letters*, *50*(23), e2023GL106715. Retrieved from https://agupubs.onlinelibrary.wiley.com/doi/abs/10.1029/2023GL106715 (e2023GL106715 2023GL106715) doi: https://doi.org/10.1029/2023GL106715

Sandhu, J. K., Yeoman, T. K., Fear, R. C., & Dandouras, I. (2016). A statistical study of magnetospheric electron density using the cluster spacecraft. *Journal of Geophysical Research: Space Physics*, *121*(11), 11,042-11,062. Retrieved from https://agupubs.onlinelibrary.wiley.com/doi/abs/10.1002/2016JA023397 doi: https://doi.org/10.1002/2016JA023397

Sandhu, J. K., Yeoman, T. K., James, M. K., Rae, I. J., & Fear, R. C. (2018). Variations of high-latitude geomagnetic pulsation frequencies: A comparison of time-of-flight estimates and image magnetometer observations. *Journal of Geophysical Research: Space Physics*, *123*(1), 567-586. Retrieved from https://agupubs.onlinelibrary.wiley.com/doi/abs/10.1002/2017JA024434 doi: https://doi.org/10.1002/2017JA024434

Sandhu, J. K., Yeoman, T. K., Rae, I. J., Fear, R. C., & Dandouras, I. (2017). The dependence of magnetospheric plasma mass loading on geomagnetic activity using cluster. *Journal of Geophysical Research: Space Physics*, *122*(9), 9371-9395. Retrieved from https://agupubs.onlinelibrary.wiley.com/doi/abs/10.1002/2017JA024171 doi: 10.1002/2017JA024171

Southwood, D., Dungey, J., & Etherington, R. (1969). Bounce resonant interaction between pulsations and trapped particles. *Planetary and Space Science*, *17*(3), 349-361. Retrieved from https://www.sciencedirect.com/science/article/pii/0032063369900683 doi: https://doi.org/10.1016/0032-0633(69)90068-3

Southwood, D. J., & Kivelson, M. G. (1981). Charged particle behavior in low-frequency geomagnetic pulsations 1. transverse waves. *Journal of Geophysical Research: Space Physics*, *86*(A7), 5643-5655. Retrieved from https://agupubs.onlinelibrary.wiley.com/doi/abs/10.1029/JA086iA07p05643 doi: https://doi.org/10.1029/JA086iA07p05643

Takahashi, K., Higbie, P. R., & Baker, D. N. (1985). Azimuthal propagation and frequency characteristic of compressional pc 5 waves observed at geostationary orbit. *Journal of Geophysical Research: Space Physics*, *90*(A2), 1473-1485. Retrieved from https://agupubs.onlinelibrary.wiley.com/doi/abs/10.1029/JA090iA02p01473 doi: https://doi.org/10.1029/JA090iA02p01473

Tsyganenko, N. A., & Sitnov, M. I. (2005). Modeling the dynamics of the inner magnetosphere during strong geomagnetic storms. *Journal of Geophysical Research: Space Physics*, *110*(A3). Retrieved from https://agupubs.onlinelibrary.wiley.com/doi/abs/10.1029/2004JA010798 doi: https://doi.org/10.1029/2004JA010798

Zhang, S., Tian, A., Degeling, A. W., Shi, Q., Wang, M., Hao, Y., ... Bai, S. (2019). Pc4-5 poloidal ulf wave observed in the dawnside plasmaspheric plume. *Journal of Geophysical Research: Space Physics*, *124*(12), 9986-9998. Retrieved from https://agupubs.onlinelibrary.wiley.com/doi/abs/10.1029/2019JA027319 doi: https://doi.org/10.1029/2019JA027319

Zhao, X. X., Hao, Y. X., Zong, Q.-G., Zhou, X.-Z., Yue, C., Chen, X. R., ... Reeves, G. D. (2021). Origin of electron boomerang stripes: Statistical study. *Geophysical Research Letters*, *48*(11), e2021GL093377. Retrieved from https://agupubs.onlinelibrary.wiley.com/doi/abs/10.1029/2021GL093377 (e2021GL093377 2021GL093377) doi: https://doi.org/10.1029/2021GL093377

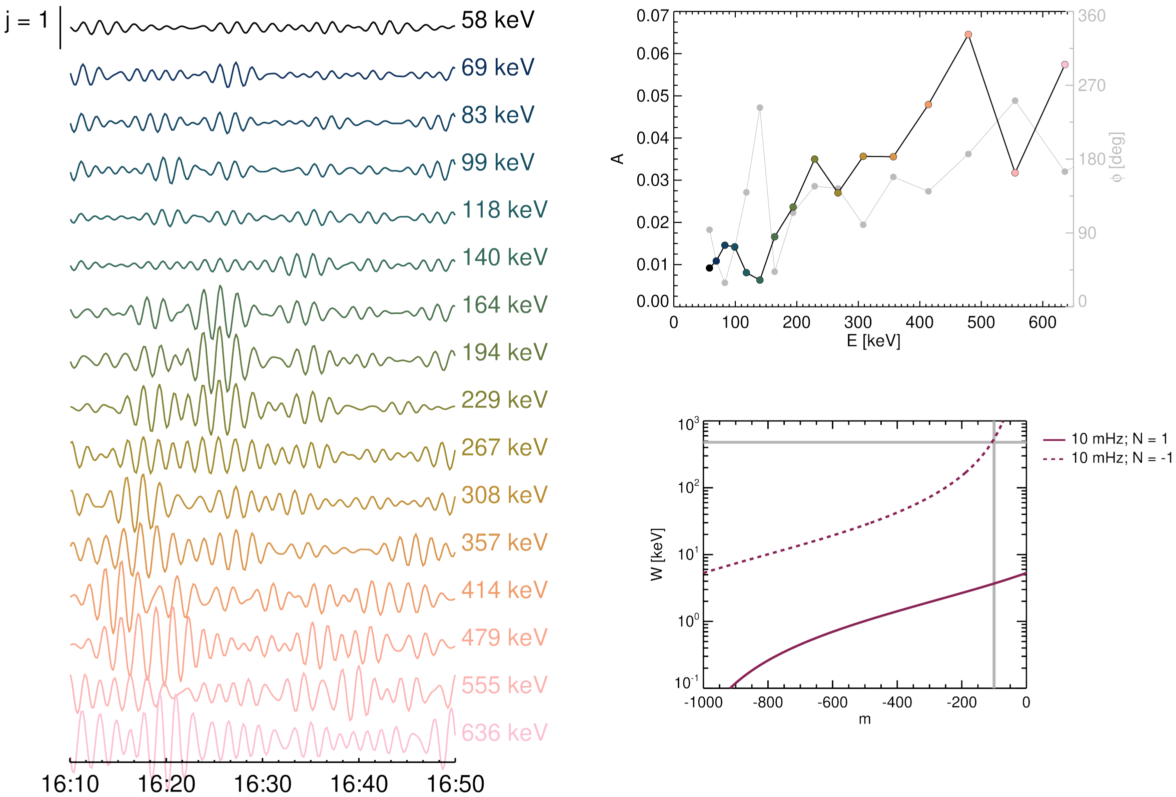

Figure S1. Panel (a) shows the proton residual flux, j, as a function of time for each energy channel, as labelled, between 16:10 to 16:50 24 June 2013. The residual flux has been bandpass filtered for frequencies between 8 to 12 mHz. The amplitude, A, and phase, ϕ [degrees], of the oscillations for each energy channel is shown in panel (b) for a 10 minute window centered on 16:17 24 June 2013. Panel (c) shows the proton energy, $W[keV]$, as a function of wavenumber, m. The solid and dashed purple lines correspond to the resonance condition for a fundamental field line resonance with a frequency of 10 mHz, as labelled. The grey lines map a proton energy of 479 keV to an estimated wave number of approximately -100.

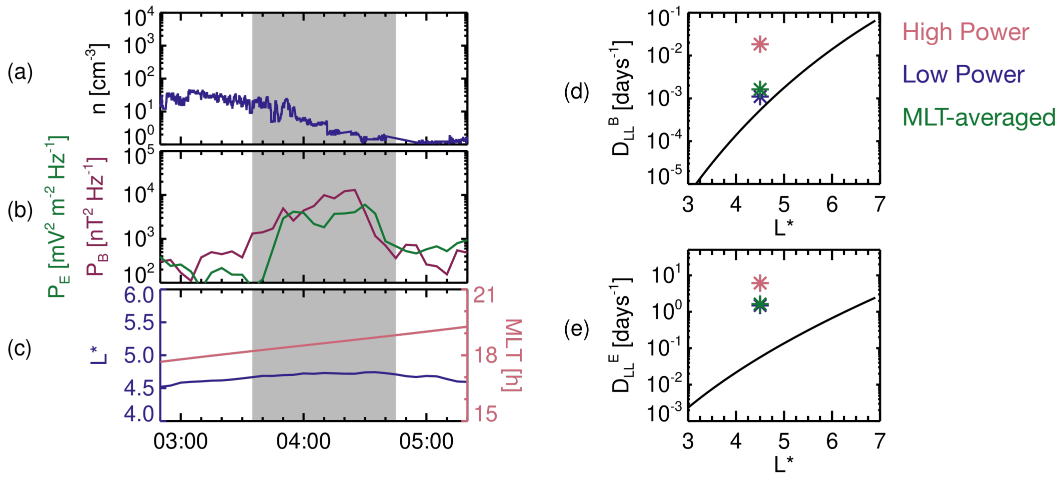

Figure S2. Time series of observations from Van Allen Probe A from 02:50 to 05:20 24 June 2015 is shown in panels (a-c), and panels (d,e) show estimated radial diffusion coefficients based on the observations. Time series are shown for (a) electron density, n [cm^{-3}], (b) power summed over 1 - 15 mHz for the compressional magnetic field (wine) and the azimuthal electric field (green), and (c) the spacecraft position in L* (indigo) and Magnetic Local Time (MLT, rose). Shaded grey regions indicate the interval of enhanced ULF wave power. Panel (d) and (e) show the magnetic radial diffusion coefficient, $D_{\mathrm{LL}}^{\mathrm{B}}$ [days^{-1}], and electric radial diffusion coefficient, $D_{\mathrm{LL}}^{\mathrm{E}}$ [days^{-1}], as a function of L*. The solid black lines correspond to the Ozeke et al. (2014) modelled diffusion coefficients. The rose and indigo asterisks indicate the estimated diffusion coefficients for spacecraft located inside and outside the plume. Panels (d,e) also include green asterisks indicating the estimated MLT-averaged diffusion coefficients, as detailed in the Supplementary Material text.